Article:

Wu, N, Jackson, CA, Johnson, HD et al. (2 more authors) (2020) Mass-transport complexes (MTCs) document subsidence patterns in a northern Gulf of Mexico salt minibasin. Basin Research, 32 (6). pp. 1300-1327. ISSN 0950-091X

https://doi.org/10.1111/bre.12429

Mass-transport complexes (MTCs) document subsidence patterns in a northern Gulf of Mexico salt minibasin

Nan Wu[1], Christopher A-L. Jackson[1], Howard D. Johnson[1], David M. Hodgson[2], Harya D. Nugraha[1]

[1]Basins Research Group (BRG), Department of Earth Science & Engineering, Imperial College, Prince Consort Road, London, SW7 2BP, UK

[2]School of Earth and Environment, University of Leeds, Leeds, LS2 9JT, UK

*Email: n.wu16@imperial.ac.uk

Abstract

Mass-transport complexes (MTCs) dominate the stratigraphic record of many salt-influenced sedimentary basins. Commonly in such settings, halokinesis is invoked as a primary trigger for MTC emplacement, although the link between specific phases of salt movement, and related minibasin dynamics, remains unclear. Here, we use high-quality 3D seismic reflection and well data to constrain the composition, geometry, and distribution (in time and space) of six MTCs preserved in a salt-confined, supra-canopy minibasin in the northern Gulf of Mexico, and to assess how their emplacement relate to regional and local controls. We define three main tectono-sedimentary phases in the development of the minibasin: (1) initial minibasin subsidence and passive diapirism, during which time deposition was dominated by relatively large-volume MTCs (c. 25 km^3) derived from the shelf-edge or upper slope; (2) minibasin margin uplift and steepening, during which time small-volume MTCs (c. 20 km^3) derived from the shelf-edge or upper slope were emplaced; and (3) active diapirism, during which time very small volume MTCs (c. 1 km^3) were emplaced, locally derived from the diapir flanks or roofs. We present a generic model that emphasises the dynamic nature of minibasin evolution, and how MTC emplacement relates to halokinetic sequence development. Although based on a single data-rich case study, our model may be applicable to other MTC-rich, salt-influenced sedimentary basins.

Keywords: MTCs, salt mini-basins evolution, Gulf of Mexico.

Introduction

Mass-transport complexes (MTCs) are deposits of subaqueous mass flows, and comprise slides, slumps, and debris-flows (Dott Jr, 1963; Nardin et al., 1979; Posamentier and Kolla, 2003). MTCs are found along all continental margins, and can play a major role in sediment transfer from the continents to the deep ocean (e.g. Masson et al., 2006; Hjelstuen et al., 2007; Talling et al., 2007; Li et al., 2015; Kioka et al., 2019). Seismic surveys image extremely large (c. 20-1100 km^3), now-buried MTCs (e.g. Gee et al., 1999; Frey Martinez et al., 2005; Moscardelli et al., 2006; Sawyer et al., 2007; Moscardelli and Wood, 2008; Sawyer et al., 2009; Ortiz - Karpf et al., 2016; Wu et al., 2019), showing they can constitute >50% of any given deep-water stratigraphic succession (Posamentier and Walker, 2006). The failure process leading to MTC emplacement can be externally preconditioned and triggered by earthquakes and oversteepening of the slope (i.e. geometric preconditioning effects) (Nisbet and Piper, 1998; O'loughlin and Lander, 2003; Masson et al., 2010; Talling et al., 2014; Clare et al., 2016). In additional to being stratigraphically important, the passage and emplacement of MTCs can damage seabed infrastructure and can trigger tsunami (Shipp, 2004; Harbitz et al., 2014). In the petroleum industry, MTCs can serve as hydrocarbon seals and/or reservoirs (e.g. Hampton et al., 1996; Locat and Lee, 2002; Weimer and Shipp, 2004; Wu et al., 2019). Therefore, understanding the origin and morphological characteristics of MTCs is important for societal and industrial reasons.

In salt-influenced sedimentary basins, uplift and subsidence associated with the flow of salt is widely considered to be the primary control on slope failure and MTC emplacement (e.g. Cashman and Popenoe, 1985; Moscardelli and Wood, 2008; Madof et al., 2009; Twichell et al., 2009; Omosanya and Alves, 2013; Yeakley et al., 2019). However, there are additional mechanisms to consider, including (i) formation of overpressure formation can be driven by fluctuations in sedimentation rate, which are influenced by the location of the minibasin relative to shelf-edge deltas and upper slope canyons; (ii) accommodation available at the time of slope failure will dictate the volume of MTC-related material that is trapped and preserved within any one minibasin, and the potential for sediment to be bypassed to more distal depocentres; (iii) erosion, and ultimately undermining and failure of the depocentre margins in response to the passage of near-bed currents (i.e. contour currents); (iv) failure of contourite bodies; (iv) fluid migration and the generation of elevated pore pressures in discrete sub-surface layers; this can reduce the vertical effective stress, thereby affecting slope stability and potentially triggering slope failure; and (v) gas hydrate dissociation, which, like pore pressure changes, can reduce sediment strength and trigger slope failure (Canals et al., 2004; Kvalstad et al., 2005; Strout and Tjelta, 2005; Masson et al., 2010; Talling et al., 2014).

Despite being volumetrically important, and although they can represent stratigraphic markers for a range of basin-related processes, MTCs are not explicitly accounted for in stratigraphic models for the salt-influenced slopes. Instead, turbidity current-fed systems dominate in these models, presumably due to their association with reservoir-prone channels and lobes, with the stratigraphic architecture and evolution of minibasins being primarily described by the fill-and-spill model (Prather et al., 1998; Winker and Booth, 2000; Booth et al., 2003; Mallarino et al., 2006; Madof et al., 2009; Prather et al., 2012). According to this model, underfilled minibasins initially trap or 'pond' sediments before being overfilled; at this point, when no more accommodation is available, sediment is bypassed to more distal depocentres (Beaubouef and Friedmann, 2000; Booth et al., 2000; Booth et al., 2003). Underlying this model are two major assumptions: (1) accommodation in the minibasin is controlled by a steady-state, longitudinal bathymetric profile, and (2) the minibasin gradient does not vary spatially and temporally during its evolution (Prather et al., 1998; Winker and Booth, 2000; Mallarino et al., 2006). However, Madof et al. (2009) and Madof et al. (2017) argue that these assumptions are unrealistic, given that minibasins can be extremely dynamic, with their geometry, subsidence rate, and accommodation changing in response to variations in sediment accumulation rate and input direction, and the rate and location of salt expulsion from beneath their subsiding depocentres.

Motivated by the above discussion, we here use 3D seismic reflection and well data from the northern Gulf of Mexico to: (i) define the geometry and emplacement mechanics of minibasin-confined MTCs; and (ii) link MTC emplacement to the development of halokinetic sequences (see below) that characterise specific stages in the relationship between minibasin subsidence and sedimentation, and diapir uplift. By doing this, we can: (i) explicitly account for MTCs in fill-and-spill models; (ii) characterise the longer-term, more dynamic interactions occurring between deep-water sedimentary systems and salt-related slope topography; and (iii) use MTCs as markers of salt-related structural deformation in deep-water. We focus on a single upper slope minibasin in the northern Gulf of Mexico (Figure 1). However, the high-quality dataset, and the fact that salt-sediment interactions have been documented in many other sedimentary basins (e.g. Gulf of Mexico, offshore Brazil, offshore West Africa and East Mediterranean), mean our findings are likely to be more broadly applicable.

Geological setting

Tectonics

The Gulf of Mexico passive continental margin formed in response to Triassic-Early Cretaceous rifting (Pindell and Dewey, 1982; Salvador, 1987; Kneller and Johnson, 2011). Rifting initiated during the Late Triassic, followed by repeated episodes of marine flooding of a confined embayment during the Middle Jurassic. This led to the accumulation of the several kilometre-thick Louann Salt (Diegel et al., 1995; Salazar et al., 2014). During the Mesozoic and Cenozoic, large volumes of sediments were shed from the North American continent. This, in concert with regional shortening, expelled the autochthonous salt into diapirs that fed a large, allochthonous salt-canopy (Galloway et al., 2000). Numerous intraslope minibasins then subsided into the canopy, in response to the differential loading by continent-derived sediment, and kinematically linked extension and shortening of the supra-salt cover (Prather, 2000). Salt tectonics has thus been a major control on the stratigraphic evolution of the northern Gulf of Mexico from the Miocene to Present (e.g. Madof et al., 2009).

Location of study area

The study area is located on the present northern Mississippi Slope, c. 60 km south-east of the modern shelf-edge (Figure 1). This covers the upper slope, in a diapir- and minibasin-rich region forming part of the larger, Plio-Pleistocene Mississippi Canyon/Fan System (Galloway et al., 2000). Present water depths range from 1150 m in the SE to 650 m in the NW. Five upper Pliocene to Holocene minibasins are imaged in our study area; we focus on the Pleistocene fill of Minibasin 5, a c. 21 km long (N-S) by c. 8 km wide (E-W) depocentre, whose base is c. 3600 m below the present seabed (Figure 2). Four salt diapirs bound the lateral margins of Minibasin 5 (A-D; Figure 2), whereas a fifth diapir underlies it (E; Figure 3).

Dataset and methods

Seismic reflection data

The seismic reflection dataset used in this study covers an area of c. 550 km^2. The dataset was acquired during 1995-1998 and reprocessed as a single survey in 2008. It contains a 3D zerophase, Kirchhoff pre-stack depth-migrated seismic reflection volume, with a vertical sample rate of 10 m, record length of 15 km, and a final bin size of 25 m x 25 m. The vertical seismic resolution is estimated to be c. 17-27 m (Wu et al., 2019).

We mapped nine key seismic horizons in a succession characterised by alternating packages of high-amplitude, continuous reflections, and low-amplitude, more chaotic reflections (Figure 3, 4). The mapped seismic horizons were selected based on their high-amplitude response and good lateral continuity, and the fact that they bound seismic-stratigraphically important packages that define specific tectono-sedimentary phases of minibasin development (see below). We mapped eight additional horizons, each of which represented the base or top surface of an MTC (e.g., H2.1, H5.1 in figure 3; see also Figures 4 and 5). We used seismic attributes (i.e. variance and chaos), generated along or between these horizons, to identify deep-water depositional elements. Variance and chaos attributes image spatial discontinuities in seismic reflection events, which could relate to important structural (e.g. intra-MTC faults) and/or stratigraphic discontinuities (e.g. the abrupt seismic facies change from seismically chaotic MTCs to more continuous slope strata) (Chopra and Marfurt, 2007; Brown, 2011).

Well data

A slightly deviated exploration well (AT-8 #1 ST) was drilled in 1997 in the east of the study area (Figure 2), encountering a c. 3600 m-thick, Pleistocene, deep-water clastic succession (Figure 3). The well-log dataset includes gamma-ray (GR) and sonic (DT) data; we used these logs to infer the lithology of the MTCs and their bounding strata via construction of a seismic-to-well tie (Figure 6) (Wu et al., 2019). Five MTC-bearing intervals were drilled and logged by AT-8 #1 ST. MTCs tend to have higher acoustic velocities and are more resistive than bounding strata (i.e. pelagic/hemipelagic deposits, turbidites) at similar burial depths (Wu et al., 2019). The MTCs are mudstone-rich, with the transported and remnant blocks they contain being relatively sandstone-rich (Wu et al., 2019).

Biostratigraphy data

Plio-Pleistocene biostratigraphic data constrain the age of strata within, above, or below the MTCs. Biostratigraphic data include planktonic foraminifera, and benthic regional and local markers, along with regional and local calcareous nannoplankton markers spanning the late Pliocene to Quaternary. Six biostratigraphic markers were identified by the contractors (see

Supplementary Material 1); we tied these to a biostratigraphic chart compiled for the Gulf of Mexico (Witrock et al., 2003). The biostratigraphic framework is based on the last occurrence or abundance acme of key biostratigraphic markers. These biostratigraphic data allow us to provide a broad, temporal framework for the main tectono-sedimentary phases of minibasin development, including the timing of MTC emplacement (see biostratigraphic data details in caption of the Figure 3, see also Supplementary Material 1-2). We note that some uncertainties exist when tying ages derived from biostratigraphic data, which are typically obtained from borehole cuttings, to seismic reflection data, for which the vertical scale is based on a conversion of two-way travel time to metres based on an understanding of subsurface velocity variations. For example, Madof et al. (2009) indicate that the real depth (in metres) of biostratigraphic datums could be higher or lower than the position of the related horizons imaged and picked in seismic reflection data. In addition, mapping of age-constrained seismic horizons away from the borehole AT-8 #1 ST across salt diapirs north and south of Minibasin 5, and across salt-related normal faults (i.e., normal faults above salt diapir E in Figure 3b), results in some uncertainties related to the local position of these horizons within the minibasin fill.

Results

Seismic facies framework

Based on reflection amplitude (e.g. high versus low) and continuity (e.g. stratified versus chaotic), we identify two main seismic facies in Minibasin 5 (Figure 5). Depositional elements and processes are further interpreted based on lithology data provided by AT-8 #1 ST, together with analogue information provided by seismic reflection- and well-based analysis of similar depositional systems in adjacent areas (e.g., Prather et al., 1998; Posamentier and Kolla, 2003; Roesink et al., 2004; Sincavage et al., 2004; Madof et al., 2009; Perov and Bhattacharya, 2011; Madof et al., 2017; Wu et al., 2019). Stratified seismic facies are characterised by good reflection continuity, and we further subdivide them based on reflection amplitude and geometry (SFs1, SFs2 and SFs3; Figure 5). Overall, stratified seismic facies document a range of non-MTC depositional elements (e.g. channels, lobes) deposited by a range of processes (e.g. turbidity currents, suspension fallout). Chaotic seismic facies are characterised by discontinuous, low- to medium-amplitude reflections, and we further subdivide them based on their internal reflection pattern (SFc1, SFc2 and SFc3; Figure 5). Overall, chaotic seismic facies record deposition within MTCs, emplaced by a range of MTC-related processes (e.g. slumps, slides, debris flows). The seismic facies defined here form the 'building blocks' for the stratigraphic fill of Minibasin 5 (see below).

Stratigraphic framework of Minibasin 5

We identified seven seismic units in Minibasin 5, comprised of the two main seismic facies (and inferred depositional elements) described above (Figure 6). Seismic unit 1 (SU-1) is c. 460-580 m thick, and consists of sandstone-rich channels and lobes, interbedded with mudstone-rich slope deposits. Seismic unit 2 (SU-2) is c. 520-600 m thick, and comprises sandstone-rich turbidite channel complexes and mudstone-rich slope deposits (Figure 6). Seismic unit 3 (SU-3) is c. 530-640 m thick, and comprises sandstone- and mudstone-rich MTCs, mudstone-rich slope sediments, and turbidite channel-fills (Figure 6). Seismic unit 4 (SU-4) is c. 210- 290 m thick and consists exclusively of mudstone-rich slope deposits. Seismic unit 5 (SU-5) is c. 470-560 m thick, and consists mudstone-rich MTCs, sandstone-rich channel complexes, and mudstone-rich slope deposits (Figure 6). Seismic unit 6 (SU-6) is c. 320-380 m thick, and contains mudstone-rich slope deposits and sandstone-rich turbidite channel complexes. The uppermost unit, Seismic unit 7 (SU-7), is c. 520-630 m thick, and consists of sandstone- and mudstone-rich MTCs, mudstone-rich slope deposits, and sandstone-rich turbidite channel complexes.

Tectono-stratigraphic development

We group the seven seismic units identified above into three age-constrained stages that define the tectono-sedimentary development of Minibasin 5 (Figure 6). These stages are defined by: (i) the geometrical characteristics of the main seismic packages (i.e. bowl- versus wedge- versus layer-shaped; see Rowan & Weimer, 1999 and Jackson et al., 2019); (ii) the way in which stratal units terminate against bounding salt diapirs, which we here describe using the composite halokinetic sequence (CHS) terminological framework of Giles and Rowan (2012); (iii) the types of depositional systems (e.g. channels, lobes, MTCs, etc.) they contains; and (iv) changes in overall sediment accumulation rate derived from well and biostratigraphic data.

Stage 1: Passive diapirism and minibasin downbuilding

Description:

Stage 1 consists of SU-1-3 and is early-middle Pleistocene. We identify two depocentres during this stage (Figure 7a). The diapirs flanking these minibasins differ in that the western one is relatively tall and has a steep margin, whereas the eastern one is of lower relief and has a more gently dipping flank (Figure 4b, 8a). The minibasin fill during this stage is bowl-shaped, with individual units progressively thinning towards and onlapping onto the flanking diapirs (i.e. tapered CHSs of Giles and Rowan, 2012) (See figure 4b and 8a). Deposition of slope channel-fills, lobes and slope sediments appear to characterise the early fill of this stage (SU-1, SU-2), although at least two seismic-scale MTCs, encased in very fine-grained slope deposits (SU-3), are identified in the upper part of the succession (Figure 6). The average sediment accumulation rate during the deposition of SU-2 was c. 844 m/Myr (Figure 9).

Interpretation:

The presence of symmetrical, bowl-shaped packages indicates Minibasin 5 initially subsided vertically and was flanked by passively rising diapirs during the early-middle Pleistocene. The presence of tapered CHSs indicates sediment accumulation rate exceeded the diapir rise rate at this time (Giles and Rowan, 2012). This high sediment accumulation rate may reflect a high sediment supply rate, which may itself reflect the proximity of the study area to the Mississippi River, which at this time delivered large volumes of sediment to upper slope minibasins (Galloway et al., 2000; Galloway, 2001) (Figure 8a) .

Stage 2: Load-driven passive salt diapirism

Description:

Stage 2 comprises seismic units 4-6 and is middle-late Pleistocene. During this stage, the northern depocentre shifts eastwards, whereas the southern depocentre simply expands areally (Figure 7b). The western diapir is flanked by tabular (SU-4-6) CHSs, whereas the eastern diapir is buried by the sediment (Figure 4b, 8b). The minibasin fill during this stage is defined by broadly wedge-shaped package (See figure 3, 4, and 8b). Slope channel-fills are deposited during the early part of this stage (SU-4), with an MTC, encased in slope mudstone (SU-5), and ultimately, slope mudstone, intercalated with slope channel-fills (SU-6). The average sediment accumulation rate increased to c. 1184 m/Myr during Stage 2 (Figure 9).

Interpretation:

During the middle-late Pleistocene, the paleo-Mississippi River continued to deliver sediments to the upper slope minibasins (Figure 8b). The presence of wedge-shaped packages records asymmetrical minibasin subsidence, and eastwards tilting of the northern minibasin (Rowan and Weimer, 1998; Hudec et al., 2009; Jackson et al., 2019). The diapir flanking the eastern side of minibasin was eventually covered by sediment, indicating an overall transition to a time when sediment accumulation rate exceeded diapir rise rate. In contrast, the western diapir continued to passively rise as the diapir rise rate exceeded sediment accumulation rate. This interpretation is supported by the observation that tabular CHSs are deposited along this diapir flank at this time (Figure 4b, 8b) (see Giles and Rowan, 2012).

Stage 3: Diapir burial, shortening, and active diapirism

Description:

Stage 3 comprises SU-7 and is late Pleistocene. During this stage, broadly layer-shaped packages were deposited (See figure 3, 4, and 8c). Overall, this package gradually thins towards yet extends across flanking salt diapirs, being thickest in the minibasin centre. However, in detail, only the lower package (containing MTC-4) extends across the diapir, with this being onlapped by an overlying package that is restricted to the minibasin centre. The upper package extends across the diapir, showing only minimal thickness changes (See figure 4b and 8c). Fine-grained slope sediments, slope channel-fills, and two MTCs are deposited during Stage 3. The average sediment accumulation rate at this time was the highest documented during the post-early Pleistocene history of minibasin, reaching up to c. 10000 m/Myr (see Figure 9).

Interpretation:

During the late Pleistocene, large amounts of sediment continued to be delivered to the upper slope and Minibasin 5 by the Mississippi River (Winker and Booth, 2000) (Figure 8c). The thickness map indicates that much of the intra-slope accommodation formed by minibasin subsidence was healed and that the flanking diapirs were buried (Figure 7c). The prevalence of layer-like stratigraphic packages (i.e. which mainly record post-welding aggradation of sediment above Minibasin 5 and its flanking diapirs) during Stage 3 reflects the high sediment accumulation (and possibly supply) rate at this time. Rowan and Weimer (1998) also interpreted that layer-shaped packages reflect relatively long-wavelength subsidence across now-welded minibasins (see also the layer-shaped package from Jackson et al., 2019).

Characterisation of Minibasin 5 MTCs

MTC 1

Description:

MTC 1 (119 km^2 and 25 km^3) is laterally and frontally confined by salt diapirs (Figure 10a, b). It is 160-190 m thick, and its NW-SE-striking, south-western lateral margin defines a sharp erosional contact between remobilised sediments (SFc3) and undeformed slope sediments (SFs1 and SFs2) (Fig. 10c). The NW-SE-striking, north-eastern lateral margin of MTC 1 is defined by the eastern salt diapir (Figure 10b). MTC 1 is sandstone-rich, containing large (130-160 m thick), internally deformed, sandstone-rich (60-80% sandstone) blocks, intercalated with thin mudstone layers (Wu et al., 2019). The highly reflective blocks, which have long axes oriented NE-SW, are directly underlain by an interval of weakly reflective, more deformed reflections (Figure 10d). NE-SW-striking, NW-dipping thrusts are observed within the blocks (Figure 10b, c, d).

Interpretation:

Deformation at the base of the blocks suggests they were transported within MTC 1 (see for example of transported blocks from Nardin et al., 1979; Bull et al., 2009a; Alves, 2015). The orientation of the NE-SW-striking thrusts, and the NW-SE-striking lateral margins, suggest that MTC 1 was transported towards the SE. We interpret the thrusts formed due to horizontal compression of the debris flow adjacent to transported blocks. An alternative interpretation is that the thrusts record shortening at the toe of the related mass movement. The lithology of the large blocks suggests MTC 1 was derived from an up-dip, sand-rich source, such as upper slope lobes and/or channels, and/or shelf-edge delta front deposits (Wu et al., 2019). The sandstone-rich blocks may therefore have travelled c. 60 km from shelf-edge/upper slope. Unfortunately, benthic foraminifera, which might help confirm the original depositional setting, or at least water depth of these sandstones, are lacking. We suggest, however, that blocks within MTC 1 are unlikely to have been derived from the nearby salt diapirs because, at this time, the diapirs were capped by an intact sedimentary roof comprising tapered CHS (see Figure 3 and 4).

MTC 2

Description:

MTC 2 (113.5 km^2 and 21.6 km^3) is 110-150 m thick and has a similar external geometry to MTC 1, being defined by: (i) a sharp, NW-SE-trending, erosional lateral margin on its south-western side, and (ii) a NW-trending diapir on its north-eastern side (Figure 11a, b). MTC 2 is mudstone-rich and contains subordinate, relatively sandstone-rich (30-40% sand) blocks that are 20-40 m thick (Wu et al., 2019). In the centre of Minibasin 5, MTC 2 contains two large (90-170 m) blocks, one of which contains mudstone-rich slope deposits at its base and sandstone-rich Slope channel deposits at its top (Figure 11c) (Wu et al., 2019). The long axes of these blocks trend NW (Figure 11b). Smaller blocks are clustered towards the north-east minibasin margin (Figure 11a, b). Unlike the transported blocks in MTC 1, blocks in MTC 2 have sharp contacts with debritic material (SFc2), are not deformed, and are not underlain by seismic-scale zones of deformation (Figure 11c).

Interpretation:

Based on the orientations of its lateral margins, we suggest MTC 2 was transported to the SE. Although there is no direct evidence indicating the source area of MTC 2 (i.e. benthic foraminifera), the presence of the subordinate sandstone-rich blocks, and similar kinematic indicators to MTC 1 (i.e. the NW-SE-trending lateral margins), together suggest MTC 2 may also have been derived from shelf-edge and/or upper slope. The seismic facies defining the blocks (i.e. concordant, moderate-amplitude, continuous seismic reflections) are similar to that of the underlying strata. The lack of deformation within these blocks implies they were *not* transported, with the absence of deformation beneath them also suggesting the substrate was *not* subjected to shear-induced deformation. Together, these two observations suggests the blocks represent undeformed substrate material that was not transported within, but is instead surrounded and capped by the MTC (i.e. 'remnant blocks'; (e.g. see examples of remnant blocks from Frey Martinez et al., 2005; Lastras et al., 2005; Posamentier and Walker, 2006; Bull et al., 2009a; Gamboa et al., 2011).

MTC 3 & 4

Description:

MTC 3 (123.5 km^2 and 20.3 km^3) is 110-160 m thick and has a similar external geometry to MTC 1 and 2, being bounded by: (i) a NW-trending trending erosional margin on its south-western side, and (ii) NW-SE-striking diapir on its north-eastern side (Figure 12a, b). MTC 3 is mudstone-dominated and contains sandstone-rich blocks (c. 20-40% sand) that are 30-60 m thick (Wu et al., 2019). Biostratigraphic data indicate MTC 3 contains transported outer shelf sediments (2377 m in well AT-8 #1 ST; Figure 13). Two biostratigraphic samples collected from a slightly deeper position (2487 m), give an age of 0.78 and 0.83 Ma (lower Pleistocene; Figure 12c, 13, see details of the biostratigraphic samples from supplementary material 1).

MTC 4 (98.4 km^2 and 18.1 km^3) has a similar geometry to the underlying MTCs, being again defined by: (i) a NW-trending lateral margin on its south-western side, and (ii) NW-SE-striking diapir on its north-eastern side (Figure 14a, b). MTC 4 is mudstone-rich and 70-110 m thick (Figure 6), and contains remnant blocks, the long axes of which trend NW (Figure 14b).

Interpretation:

The orientations of their lateral margins suggest that MTC 3 and 4 were transported towards the SE (e.g. Frey Martinez et al., 2005; Bull et al., 2009a). MTC 3 contains direct biostratigraphic evidence that it was derived from the paleo shelf-edge (i.e. transported outer shelf facies sample; Figure 13). The presence of two different age samples (0.78 and 0.85 Ma) from the same depth (2478 m) within MTC 3 is intriguing. This might indicate that MTC 3, emplaced at 0.78 Ma, entrained older (i.e. 0.83 Ma) substrate (i.e. seabed) material during transport and emplacement (Figure 12d). An alternative interpretation is that the slightly old (i.e. 0.83 Ma) material was shed from the roof of a growing diapir flanking the minibasin, and reworked into the younger (i.e. 0.78 Ma) MTC 3 (Figure 12e). Because MTC 4 is similar to older MTCs in terms of its geometry and kinematics, we infer it was also likely derived from the upper slope or paleo shelf-edge.

MTC 5

Description:

MTC 5 (29.07 km^2 and 2.6 km^3) is 110-180 m thick and was deposited in the centre of Minibasin 5, being bounded by diapirs on its NE and W side, and a salt-cored structure high on its SE side (Figure 15a, b). MTC 5 is sandstone-rich and is intercalated with thin mudstone layers. Sandstone-rich blocks (c. 40-60% sand) that are 60-90 m thick occur within MTC 5. We sub-divide MTC 5 into MTC 5.1 and MTC 5.2, based on cross-cutting relationships between the lateral margins of the two units, with MTC 5.2 being slightly younger than MTC 5.1 (Figure 15b, d). MTC 5.1 is delineated by a set of NE-SW-striking normal faults and NE-SW-striking thrusts in its proximal and distal parts, respectively (Figure 15b, 15c). MTC 5.2 has a NE-trending headwall scarp, being bound by NW-SE-striking lateral margins. Well AT-8 #1 ST intersected MTC 5.1, showing the deposit is sandstone-rich (Figure 6). However, well AT-8 #1 ST does not penetrate MTC 5.2, thus its lithology is unknown.

Interpretation:

The strike of the normal faults and thrusts suggest the bulk movement of MTC 5.1 was towards the E (e.g. Frey Martinez et al., 2005; Bull et al., 2009a). The orientation of the headwall scarp and lateral margins suggest that MTC 5.2 was transported to the SE (e.g. Bull et al., 2009a). The confined nature of MTC 5.1 and 5.2 suggest they were both sourced from locally positive topography generated by the growth of an underlying salt diapir.

MTC 6

Description:

MTC 6 (18.9 km^2 and 1.13 km^3) is located just below the seabed along the south-eastern flank of salt diapir A (Figure 16a, b). MTC 6 has well-defined, NW-trending lateral margins and is 50-70 m thick. In the up-dip part of MTC 6, N-S-striking normal faults occur on the flank of the diapir, with hangingwall strata thickening towards and documenting syn-sedimentary growth of the normal faults (Figure 16c). N-S-striking thrusts are also developed near the north-eastern lateral margin of MTC 6; this margin is erosional, with the magnitude of erosion increasing towards the northeast (Figure 16a, b). MTC 6 pinches-out to the southwest (Figure 16d). The N-S-striking normal faults and thrusts are present above the main body of MTC 6 (Fig. 16e). AT-8 #1 ST does not penetrate MTC 6, thus its lithology is unknown.

Interpretation:

The orientations of the normal faults and the lateral margins suggest MTC 6 was transported to the SE. These spatial relationships suggest that MTC 6 was triggered by gravity-driven instability of the seabed, driven by (relative) uplift of the seabed by diapir A. The emplacement of MTC 6 created an exposed and unstable lateral margin along its NE side

(Figure 16d, 17 a). This margin thus collapsed, depositing material on top of the main body of the MTC 6 (Figure 16e, 17b).

Discussion

Origin and classification of MTCs

Moscardelli and Wood (2008) classified MTCs as 'attached' (i.e. relatively far travelled, having originated from the shelf-edge or upper slope) when the length: width ratio is >4; and 'detached' (i.e. having originated from and being still partly physically connected to, a local source, such as a salt-cored structural high) when the length: width ratio is <4. Based on the degree of internal deformation and morphology, Gamboa and Alves (2016) further classify detached MTCs into Type 1 (i.e. highly deformed, with the length of the headwall: distance to toe <1, and with their long axes parallel to the transport direction) and Type 2 (i.e. less deformed, with the length of the headwall: distance to toe >1, and with their long axes perpendicular to the transport direction). Because our data do not image their full extent, the maximum length and width of the extrabasinal MTCs (MTC 1-4), the headwall length and distance to toe length of intrabasinal MTC 5 remain unknown. Therefore, we cannot apply the schemes of Moscardelli and Wood (2008) and Gamboa and Alves (2016), and instead use morphometric and biostratigraphic data to classify our MTCs and to deduce if they were derived locally or from beyond the minibasin. We here provide additional guidelines on how to differentiate between attached and detached MTCs in salt-confined minibasin settings, focusing on: (i) MTC morphometrics (i.e. external geometry, area, volume); (ii) the composition and age of the MTCs; and (iii) the geometrical relationship between the MTCs and bounding salt diapirs. We classify MTCs in such salt-influenced settings into: (i) shelf-edge/upper slope derived MTCs and (ii) diapir-derived MTCs (Figure 18).

Shelf-edge/upper slope derived MTCs (MTC 1-4)

The shelf-edge-/upper slope-derived MTCs, sourced from the collapse of coeval shelf-edge deltas, and/or supplied by reworked upper slope channels and lobes, tend to be, overall, larger than the diapir-derived MTCs (i.e. 110-270 m thick; 113.5-123.5 km^2 in area; 20.3-25.1 km^3 in volume). Shelf-edge-/upper slope-derived MTCs can be sandstone- or mudstone-rich, and typically contain sandstone-rich blocks. Emplacement of these types MTC appear most common during the initial phase of minibasin development, at a time when sediment accumulation rate exceeded the rise rate of bounding passive diapirs (i.e. Stage 1 and 2; early to middle Pleistocene) (Figure 19). In this salt-tectonic context, the lack of diapir-derived MTCs is logical, given that at this time diapirs were unable to build sufficient differential relief (i.e. topography) or steep slopes to trigger slope failure. The shelf-edge-/upper slope-derived MTCs are thickest near the minibasin centre and were transported towards the SE, along a bathymetric low laterally bound by salt diapirs; slope morphology controlled sediment dispersal and ultimate preservation, even if it was not responsible for locally supplying sediment. The trigger for slope failure and MTC emplacement is unknown.

The shelf-edge/upper slope-derived MTCs in Minibasin 5 are similar in terms of their location, volume, and source area to so-called ‘regional’ or ‘extra-basinal’ MTCs described from other minibasins (Madof et al., 2009; Doughty-Jones et al., 2019). More specifically, these MTCs: (i) extend across the full width of the minibasin in which they are preserved, and occur in the lowermost (i.e. earliest) part of the minibasin fill; (ii) are large in terms of their area and volume when compared to diapir-derived or ‘local’ MTCs; and (iii) are sourced from the outer-shelf and can contain outer-shelf bio-facies.

Diapir-derived MTCs (MTC 5-6)

Diapir-derived MTCs tend to be smaller than shelf-edge-/upper slope-derived MTCs (i.e. 50-90 m thick; 18.9 to 29.7 km^2 in area; 1.13 to 2.6 km^3 in volume). Diapir-derived MTCs were emplaced during the latter stage of minibasin development, when the rate of diapir rise appeared to have exceeded the rate of sediment accumulation (Stage 3; late Pleistocene) (Figure 19). These MTCs are preserved on or immediately downdip of, the flanks of diapirs (i.e. MTC 6), or on local topographic highs above buried diapirs (i.e. MTC 5). Diapir-derived MTCs are thickest near diapir margins and thin downdip into the minibasin centres, indicating local derivation from above or the flanks of diapir-cored structural highs. It is likely that the preconditioning and triggering of this type of MTC is linked to localised gravitational instability, more specifically oversteepening of diapir flanks during passive or active diapirism (discussed below).

The diapir-derived MTCs in Minibasin 5 are comparable to so-called ‘intra-basinal’ or ‘local’ MTCs described from other minibasins (Beaubouef et al., 2003; Owen et al., 2007; Madof et al., 2009; Gamboa and Alves, 2016; Doughty-Jones et al., 2019). More specifically, these types of MTC are: (i) preserved adjacent to the diapir from which they are sourced; (ii) are relatively small in terms of their volume and areal extent; and (iii) developed in the uppermost (i.e. latest) part of the minibasin fill, because at this time significant diapir-related structural relief was developing around the minibasin margins.

Preconditioning factors and triggers for emplacement of minibasin-constrained MTCs

Eustasy

Eustasy controls depositional processes and stratal patterns occurring in sedimentary basins (e.g., Vail et al., 1977; Posamentier et al., 1988; Catuneanu, 2002; Posamentier and Kolla, 2003; Catuneanu et al., 2011). Eustacy was particularly important during the Pleistocene in the northern Gulf of Mexico, when rapid (c. 500 years), high-amplitude (>100 m) sea-level fluctuations resulted in rapid margin progradation and retrogradation (Galloway, 2001). For example, Pleistocene sea level fluctuations are known to have caused major changes in the position of the paleo-coastline (>100 km) during glacial intervals (Galloway et al., 2011). During periods of sea-level fall, sediment supply was so high that deltas could reach the shelf-edge. Rapid progradation during periods of sea-level fall and lowstand could increase pore-fluid pressure within underlying, very fine-grained sediment, because these low intervals could not efficiently expel their pore water when loaded by thick, shelf-edge deltas (Madof et al., 2017). This primed or preconditioned the shelf-edge or upper slope to fail, or could even trigger failure, resulting in the emplacement of shelf-edge/upper slope-derived MTCs (Posamentier and Kolla, 2003). During periods of relatively rapid sea-level rise, transient excess pore pressures could be generated in low-permeability sediment, decreasing slope stability, and potentially triggering slope failure and the emplacement of upper slope-derived MTCs (Smith et al., 2013).

There were numerous and frequent, glacio-eustatic sea-level fluctuations during the Pleistocene in the Gulf of Mexico (Figure 20). It is thus be appealing to link MTC emplacement to periods of falling and lowstands of sea level, via the causal mechanism outlined above. However, we note there were many more sea-level falls and lowstands than there are seismically resolvable MTCs in Minibasin 5. Any MTCs generated during periods of sea-level fall may have: (i) been ponded in up-dip minibasins; (ii) transformed into turbidity currents and bypassed Minibasin 5, being instead preserved in downdip minibasins; and (iii) been emplaced in minibasins lateral to Minibasin 5. An alternative interpretation is that sea-level variations and gravity-driven deep-water sedimentation are completely unrelated (Maslin et al., 1998; Smith et al., 2013; Urlaub et al., 2013; Clare et al., 2014; Pope et al., 2015; Coussens et al., 2016). In this case, other factors, such as sedimentation rate changes, fluid migration, and salt diapirism, need to be considered.

Sedimentation

MTC emplacement may have been controlled by fluctuations in sediment supply; i.e. during periods of high supply, which may have been climatically controlled, deltas may have reached the shelf-edge even during highstands, before collapsing to supply MTCs. In the northern Gulf of Mexico, Pleistocene sedimentation rates were extremely high, and more than double Pliocene rates (Molnar, 2004). This increase reflects entrenchment and greater discharge of the Mississippi River, related to its capture of the Ohio and Missouri rivers (Galloway et al., 2011). The reorganisation of the Mississippi River System resulted in a significant sediment supply increase and led to the development of submarine canyons that incised the shelf, especially during periods of glacial retreat (Galloway et al., 2000; Rittenour et al., 2007; Galloway et al., 2011; Bentley Sr et al., 2016). High sediment input from the Mississippi River also caused rapid shelf-edge delta progradation; this could have increased delta-front instability, and triggered sediment gravity currents (e.g., Sydow et al., 2003; Moscardelli et al., 2006). We consider that the high sedimentation rates associated with paleo-Mississippi River System were a key factor in preconditioning the shelf-edge/upper slope derived MTCs in the study area.

Geometric preconditioning (oversteepening)

Minibasins are surrounded by diapirs that can rise and deform the overlying free surface. If the related slope becomes sufficiently steep it can fail, triggering the emplacement of diapir-derived MTCs (Cashman and Popenoe, 1985; Tripsanas et al., 2004; Madof et al., 2009; Hill et al., 2011; Giles and Rowan, 2012). However, if the slope steepens relatively slowly, the increase in steepness would take a long duration to passes a critical threshold and cause a slope failure. In this case, the decomposition of gas hydrates or fluid migration (discussed below) might accelerate the process, account for the preconditions and triggers of diapir derived MTCs.

Fluid migration

The headwalls (i.e. where MTCs initiate, Bull et al., 2009a) of MTCs are most abundant on slopes, in water depths of 1000-1500 m (or even deeper; e.g. Weaver et al., 2000; McHugh et al., 2002; Hühnerbach and Masson, 2004), rather than close to the shelf-edge where the sedimentation accumulation rates are highest. This suggests that sediment accumulation rate (and perhaps related sea level fluctuations) are not the key control on the preconditioning and triggering of upper-slope and minibasin-derived MTCs. Instead, fluid migration may play an important role. More specifically, fluid could migrate to the upper slope along permeable horizons that extend updip from the lower slope, with this sudden influx of fluids generating excess pore pressure, thereby decreasing sediment shear strength and slope stability (Dugan and Flemings, 2000; Masson et al., 2010).

Gas hydrate dissociation

Gas hydrates are common in shallowly buried (0-600 m below seabed) sediments in the northern Gulf of Mexico (MacDonald et al., 1994; Milkov and Sassen, 2001; Boswell et al., 2012). The dissociation of solid gas hydrate (the loss of free gas and water) may lead to rapid sediment compaction and can generate excess pore pressures (Grozic, 2010). The process of hydrate dissociation can also generate freshwater, which could play a role in leaching mud-rich sediments, thereby increasing the quick clay behaviour of the mud-rich sediments (Bull et al., 2009b). Gas hydrate dissociation could thus prime the slope to fail, and ultimately trigger slope failure and MTC emplacement (e.g. the Storegga slide in Norway, Bryn et al., 2005). Gas hydrates can be structurally focused above supra-salt faults that act as conduits for the upward migration of deeply generated thermogenic gas into the shallower, gas hydrate stability zone. As unstable gas hydrates normally occur 300-900 m below the seafloor (Mienert et al., 2005), diapir-derived (in addition to shelf-edge/upper slope-derived) MTCs could also genetically related to the process of gas hydrate dissociation.

Seismicity

The study area is located along a relatively tectonically quiescent passive margin, in an area generally regarded as having low overall seismicity (Franco et al., 2013). However, significant seismic activity does locally and intermittently occur, with spatially variable peak ground accelerations due to differential amplification and/or attenuation by the basin-fill. For example, in 1978 a magnitude Mw=5.0 earthquake, triggered by an intraplate tectonic event, occurred near central-northern Gulf of Mexico (Frohlich, 1982). A larger, magnitude Mw=5.9 event, which may have been triggered by the tectonic loading of the salt and its overburden, took place in a nearby region in 2006 (Gangopadhyay and Sen, 2008). Smaller earthquakes could also be triggered by increasing differential stresses related to the relatively high sediment accumulation rates characterising the Pleistocene phase of Minibasin 5 (see example from Lofoten and Norway Basins, Byrkjeland et al., 2000). Seismicity could therefore trigger emplacement of the shelf-edge/upper slope- and diapir-derived MTCs encountered in the study area.

The link between composite halokinetic sequences and MTCs

Halokinetic sequences are defined as “unconformity-bound packages of thinned and deformed strata adjacent to passive diapirs” (Rowan et al., 2003). Halokinetic sequences record cycles of passive and minor active diapirism, when salt periodically rises and pierces the diapir roof (Rowan et al., 2003). Halokinetic sequences form as the rate of net vertical diapiric rise varies relative to the local rate of sediment accumulation (Giles and Lawton, 2002; Rowan et al., 2003). Within this conceptual framework, diapir-derived MTCs are most likely to be emplaced in tabular composite halokinetic sequences, being generated by break-up of the diapir roof, during a period when the diapir rise rate exceeds the sediment accumulation rate (Giles and Rowan, 2012). Diapir-derived MTCs are thought to only extend a few hundred metres away from their source diapirs (i.e. diapir-derived MTCs from Giles and Rowan, 2012; Hearon et al., 2014).

Our observations are consistent with the outcrop--based model of Giles and Rowan (2012), in that the intra-basinal MTCs (diapir-derived MTCs) are best-developed in Stage 3, when tabular CHSs were deposited. However, we show that diapir-derived MTCs (i.e. MTC 6) can extend significant distances (> 8 km) away from their source diapir. During the initial stage of subsidence of Minibasin 5, when sediment accumulation rate exceeded diapir rise rate and diapir-derived MTCs were accordingly absent, salt diapirs only provided the physical bounding constraints for the distribution of extra-basinal MTCs (e.g. MTC 1 and 2); diapiric rise played no role in triggering slope failure and MTC emplacement. Thus, during different stages of the evolution of a minibasin, halokinetic sequences could have different relationships with their associated MTCs.

Minibasin evolution; beyond the fill-and-spill model

The widely adopted fill-and-spill model has two key assumptions: (i) the longitudinal gradient between two (or more) adjacent minibasins does not vary through time; and (ii) sedimentation rate always exceeds the rate of minibasin subsidence (Beaubouef and Friedmann, 2000; Booth et al., 2000; Booth et al., 2003). In fact, the fill-and-spill model essentially views slope depocentres as being static.

Several studies show that the longitudinal gradients and the seabed bathymetry changes through time because minibasins are dynamic not static, meaning the ratio of the rate of accommodation creation to sediment supply/accumulation can be highly variable (e.g. Madof et al., 2009; Sylvester et al., 2015; Madof et al., 2017). The original fill-and-spill model is thus overly simplistic. Madof et al. (2017) propose a process-driven model of 'subsidence and margin failure' for minibasin evolution; this better accounts for the seismic-stratigraphic architecture of minibasins compared to the fill-and-spill model. In their model, rising diapirs pond sediments within minibasins (Stage 1). The ponded sediments then promote minibasin subsidence (due to density-driven downbuilding) and basin margin uplift (due to passive diapirism) (Stage 2). Margin uplift leads to slope oversteepening, failure, and generation of intra-basinal MTCs (Stage 3). Although this model is suitable for intra-basinal MTCs (i.e. derived from salt minibasin margins), it does not address how extra-basinal, shelf-edge-/upper slope-derived MTCs are emplaced in minibasins. Thus, we here extend their model by taking halokinesis, subsidence and sedimentation into consideration, using our observations from the northern Gulf of Mexico, in which MTCs constitute c. 60% of the minibasin fill.

We have identified three key stages during the evolution of Minibasin 5: (i) *Stage 1* – this stage was characterised by relatively low sediment accumulation rates (c. 844 m/Myr) (Figure 20), passive diapirism, and broadly vertical subsidence of the minibasin; although sediment accumulation rates were relatively low, they were high relative to the rise rate of the bounding diapirs, resulting in the deposition of tapered CHSs. Sand-rich slope channel complexes and lobes, as well as sand-rich, shelf-edge/upper slope-derived MTCs, were deposited in the minibasin at this time (Figure 19). These extra-basinal MTCs were relatively large (i.e. 25 km^3) in relation to the minibasin size, and were deposited in the deepest, central point of the minibasin. MTC emplacement was associated with substantial substrate deformation; (ii) *Stage 2* – this stage was characterised by relatively high sedimentation rates

(c. 1184 m/Myr) (Figure 20), during which time the rise rate of passive diapirs exceeded the sediment accumulation rate, resulting in the deposition of tabular CHSs. Mud-rich, shelf-edge-derived MTCs (i.e. MTC 3), sand-rich slope-channel fills, and mud-rich slope deposits were deposited during Stage 2 (Figure 19). Stage 2 MTCs are geometrically similar to Stage 1 MTCs, but were smaller (i.e. 1.13km^3); (iii) *Stage 3* - this final stage was characterised by very high sediment accumulation rates (c. 10000 m/Myr) (Figure 20) that exceeded the rate of diapir rise, resulting in capping of the minibasin-bounding diapirs by a relatively thick roof. Stage 3 saw deposition of sand-rich slope-channel fills and lobes, and sand-rich, diapir-derived MTCs (Figure 19). These relatively small (i.e. 1.13km^3), intra-basinal MTCs were sourced from and deposited proximal to, the flanks of rising salt diapirs.

Our model develops the model of Madof et al. (2009), showing that: (i) the interplay between the relative rate of salt diapir rise, minibasin subsidence, and sediment accumulation rate dictates minibasin seismic-stratigraphic or stratigraphic architecture; (ii) MTCs are a key stratigraphic element of marine minibasins; and (iii) the style of salt-related structural deformation can be determined by the volume and type of coeval MTCs.

Conclusions

1. We use seismic reflection and well data to identify six MTCs in a Pleistocene, supra-canopy minibasin in the northern Mississippi slope, northern Gulf of Mexico.
2. We identify two types of MTC that differ in their geometry, volume, and source area: (i) relatively large (98.4-123 km^2 in area, 18.1-25 km^3 in volume, 110-270 m in thickness), shelf-edge/upper slope-derived, extra-basinal MTCs; (ii) relatively small ((18.9-29.7 km^2 in area, 1.13-2.6 km^3 in volume, 50-90 m in thickness), diapir-derived MTCs, intra-basinal MTCs.
3. Shelf-edge/upper slope-derived MTCs were preferentially deposited during the earlier phase of minibasin development when sediment accumulation rates exceeded diapir rise rates. During this time, diapirs only constrained the distribution of shelf-edge/upper slope-derived MTCs; they were not involved in the triggering of these deposits. Diapir-derived MTCs were mainly deposited during the late stage of minibasin development, at a time when salt diapir rise rate was lower than sediment accumulation rate.

4. We present a model for minibasin development that highlights the role of MTCs and develops the widely applied fill-and-spill model. More specifically, our models stresses: (i) the interplay between the relative rate of salt diapir rise, minibasin subsidence, and sediment accumulation rate dictates minibasin seismic-stratigraphic or stratigraphic architecture; (ii) that MTCs are a key stratigraphic element of marine minibasins; and (iii) the style of salt-related structural deformation can be determined by the volume and type of coeval MTCs.

Figure Captions

Figure 1. Location map of the study area relative to the globe map (left) and the study area (right), showing the position of the modern shelf-edge (black dotted line), paleo-shelf-edge (white dotted line), and modern depositional systems. The location map is combined with bathymetry (coloured) and northern Gulf Coastal Plain topography (blue and white) of the Gulf of Mexico region. The study area (see yellow box) is located in the upper continental slope of the northern Gulf of Mexico along the SW distal edge of the Mississippi Canyon. The location of the Pleistocene-shelf edge is from Galloway et al. (2011), the Northern Gulf of Mexico Deepwater Bathymetry map is modified from The Bureau of Ocean Energy Management (BOEM).

Figure 2. Depth map (Depth below seabed) for top salt, showing the overall salt-tectonic structure of the study area. 1-5 and A-C refer to minibasins and salt structures, respectively, described in the text. See location from Figure 1.

Figure 3. (a) N-trending un-interpreted seismic section. (b) Interpreted N-trending seismic section showing the overall salt-tectonic structure of the study area, the nine key seismic horizons (H0 to seabed) and main MTC-bearing intervals (MTC 1 to MTC 6). See location from figure 2. The biostratigraphic framework is based on the last occurrence or abundance acme of key biostratigraphic markers. The details of the biostratigraphic data colorations are as follows: the last occurrence of the early Pleistocene nannoplankton, *Scyphosphaera pulcherima* (~1.92 Ma; Siesser, 1998; Young, 1998), correlates with our seismic horizon H0.

The abundance acme of the early Pleistocene planktonic foraminifera, *Sphaeroidinella dehiscens acme B* (~1.62 Ma; Waterman et al., 2015), correlates with our seismic horizon H1. The last occurrence of the early Pleistocene planktonic foraminifera, *Sphaeroidinella dehiscens acme A* (~0.85 Ma; Waterman et al., 2015), correlates with our seismic horizon H3. The last occurrence of the early Pleistocene calcareous nannoplankton, *Pseudoemiliania lacunosa C (~0.83 Ma; Waterman et al., 2015)*, correlates with our seismic horizon H5. The last occurrence of the Late Pleistocene planktonic foraminifera, *Globorotalia flexuosa (~0.07 Ma; Waterman et al., 2015)*, correlates with our seismic horizon H7.

Figure 4. (a) W-trending un-interpreted seismic section. (b) Interpreted W-trending seismic section showing the overall salt-tectonic structure of the study area, the nine key seismic horizons (H0 to seabed) and main MTC-bearing intervals (MTC 1 to MTC 5). See location from Figure 2, and the details of the biostratigraphic data colorations from Figure 1 caption.

Figure 5. Main seismic facies summary, with seismic section of six seismic facies recognized in the study area, a brief interpretation of the seismic facies, log facies, lithology, and facies characteristics. See the text for detailed descriptions.

Figure 6. Correlation charts for the study area showing well logs (GR, Sonic, and ATR), interpreted lithology, well correlated seismic section, key horizons, and geological age of each episodes.

Figure 7. (a) Thickness map between horizon H0 and horizon H4, showing: (i) the thickness variation of minibasin evolution stage 1; and (ii) the southern and northern depocentres (labelled number 1 and 2). (b) Thickness map between horizon H4 and horizon H7, showing: (i) the thickness variation of minibasin evolution stage 2; and (ii) the southern and northern depocentres (labelled number 1 and 2). (c) Thickness map between horizon H7 and horizon seabed, showing the thickness variation of minibasin evolution stage 3.

Figure 8. Cartoons of Minibasin 5 evolution model: (a) Passive diapirism and minibasin down-building; (b) Load-driven passive salt diapirism; (c) Diapir burial, shortening, and active diapirism.

Figure 9. Burial curve of Minibasin 5, the curve is plotted against the corresponding true vertical depth. The horizontal axis representing the age and the vertical axis representing the

depth (sediment thickness), showing three stages of minibasin evolution. The average sedimentation rates are estimated by the total thickness of the sediments deposited in each stage divided by the time gap: (i) Stage 1 – c. 844 m/Myr; Stage 2 – c. 1184 m/Myr; Stage 3 – c. 10000 m/Myr.

Figure 10. (a) Variance attribute calculated for the interval between the H2 and H2.1 seismic horizons, showing the plain view of MTC 1; (b) Sketch of MTC 1 indicating key kinematic features associated with MTC 1; (c) E-W oriented seismic section of MTC 1, see location from Figure 10a; (d) NW-SE trending seismic section of MTC 1, see location from Figure 10a.

Figure 11 (a) Variance attribute calculated for the interval between the H3 and H4 seismic horizons, showing the plain view of MTC 2; (b) Sketch of MTC 2 indicating key features associated with this MTC; (c) SE-NW oriented seismic section of MTC 2, see location from figure 11a.

Figure 12 (a) Chaos attribute calculated for the interval between the H5 and H5.1 seismic horizons, showing the plain view of MTC 3; (b) Sketch of MTC 3 indicating key features associated with this MTC; (c) SW-NE oriented seismic section of MTC 3, see location from Figure 12a; (d) Sketch of MTC 3 showing that the origin of this MTC is from the shelf-edge; (e) Sketch of MTC 3 showing that the emplacement process of MTC 3 is influenced by the uplift of salt diapirs.

Figure 13. Biostratigraphy data compilation showing the age of six MTCs bearing intervals in the study area.

Figure 14 (a) Variance attribute calculated for the interval between the H7.1 and H7.2 seismic horizons, showing the map view of MTC 4; (b) Sketch of MTC 4 indicating key features associated with this MTC.

Figure 15 (a) Variance attribute calculated for the interval between H7.3, H7.4 seismic horizons, showing the map view of MTC 5; (b) Sketch of MTC 5 indicating key features associated with this MTC; (c) NE-SW trending seismic section of MTC 5, see location from Figure 15a; (d) SW-NW-NW trending seismic section of MTC 5, see location from Figure 15a.

Figure 16 (a) Variance attribute calculated for the interval between the H7.5 and H7.6 seismic horizons, showing the map view of MTC 6; (b) Sketch of MTC 6 indicating key features associated with this MTC; (c) SE-NW trending seismic section of MTC 6, see location from Figure 16a; (d) SW-NE trending seismic section of MTC 6, see location from Figure 16a; (e) S-N trending seismic section of MTC 6, see location from Figure 16a.

Figure 17 (a) Sketch of MTC 6 showing the first stage of the emplacement; (b) Sketch of MTC 6 showing the second stage of the emplacement.

Figure 18. Schematic 3D view of three different types of MTCs observed around the study area: (i) Shelf-edge derived MTCs (SED); (ii) Upper slope derived MTCs (USD); and (iii) Diapir-derived MTCs (DD).

Figure 19. Conceptual model for extrabasinal MTCs, intrabasinal MTCs, slope channels, and background slope sediments.

Figure 20. Eustatic sea level curve for Pleistocene and Holocene correlated with general age of the MTCs, modified from Imbrie et al. (1984); and the sedimentation rates curve through time during different stage of minibasin evolution.

Reference

Alves, T. M., 2015, Submarine slide blocks and associated soft-sediment deformation in deep-water basins: a review: Marine and Petroleum Geology, v. 67, p. 262-285.

Beaubouef, R., V. Abreu, J. Van Wagoner, H. Roberts, N. Rosen, R. Fillon, and J. Anderson, 2003, Basin 4 of the Brazos–Trinity slope system, western Gulf of Mexico: the terminal portion of a late Pleistocene lowstand systems tract: Shelf margin deltas and linked down slope petroleum systems: Global significance and future exploration potential: Proceedings of the 23rd Annual Research Conference, Gulf Coast Section SEPM Foundation, p. 45-66.

Beaubouef, R., and S. Friedmann, 2000, High resolution seismic/sequence stratigraphic framework for the evolution of Pleistocene intra slope basins, western Gulf of Mexico: depositional models and reservoir analogs: Deep-water reservoirs of the world: Gulf Coast Section SEPM 20th Annual Research Conference, p. 40-60.

Bentley Sr, S., M. Blum, J. Maloney, L. Pond, and R. Paulsell, 2016, The Mississippi River source-to-sink system: Perspectives on tectonic, climatic, and anthropogenic influences, Miocene to Anthropocene: Earth-Science Reviews, v. 153, p. 139-174.

Booth, J., A. DuVernay III, D. Pfeiffer, and M. Styzen, 2000, Sequence stratigraphic framework, depositional models, and stacking patterns of ponded and slope fan systems in the Auger Basin: Central Gulf of Mexico slope: Perkins Research Conference, p. 82-103.

Booth, J. R., M. C. Dean, A. E. DuVernay III, and M. J. Styzen, 2003, Paleo-bathymetric controls on the stratigraphic architecture and reservoir development of confined fans in the Auger Basin: central Gulf of Mexico slope: Marine and Petroleum Geology, v. 20, p. 563-586.

Boswell, R., T. S. Collett, M. Frye, W. Shedd, D. R. McConnell, and D. Shelander, 2012, Subsurface gas hydrates in the northern Gulf of Mexico: Marine and Petroleum Geology, v. 34, p. 4-30.

Brown, A. R., 2011, Interpretation of three-dimensional seismic data, Society of Exploration Geophysicists and American Association of Petroleum Geologists.

Bryn, P., K. Berg, C. F. Forsberg, A. Solheim, and T. J. Kvalstad, 2005, Explaining the Storegga slide: Marine and Petroleum Geology, v. 22, p. 11-19.

Bull, S., J. Cartwright, and M. Huuse, 2009a, A review of kinematic indicators from mass-transport complexes using 3D seismic data: Marine and Petroleum Geology, v. 26, p. 1132-1151.

Bull, S., J. Cartwright, and M. Huuse, 2009b, A subsurface evacuation model for submarine slope failure: Basin Research, v. 21, p. 433-443.

Byrkjeland, U., H. Bungum, and O. Eldholm, 2000, Seismotectonics of the Norwegian continental margin: Journal of Geophysical Research: Solid Earth, v. 105, p. 6221-6236.

Canals, M., G. Lastras, R. Urgeles, J. Casamor, J. Mienert, A. Cattaneo, M. De Batist, H. Haflidason, Y. Imbo, and J. Laberg, 2004, Slope failure dynamics and impacts from seafloor and shallow sub-seafloor geophysical data: case studies from the COSTA project: Marine Geology, v. 213, p. 9-72.

Cashman, K., and P. Popenoe, 1985, Slumping and shallow faulting related to the presence of salt on the continental slope and rise off North Carolina: Marine and Petroleum Geology, v. 2, p. 260-271.

Catuneanu, O., 2002, Sequence stratigraphy of clastic systems: concepts, merits, and pitfalls: Journal of African Earth Sciences, v. 35, p. 1-43.

Catuneanu, O., W. E. Galloway, C. G. S. C. Kendall, A. D. Miall, H. W. Posamentier, A. Strasser, and M. E. Tucker, 2011, Sequence stratigraphy: methodology and nomenclature: Newsletters on stratigraphy, v. 44, p. 173-245.

Chopra, S., and K. J. Marfurt, 2007, Seismic attributes for prospect identification and reservoir characterization, Society of Exploration Geophysicists and European Association of Geoscientists and Engineers.

Clare, M. A., J. H. Clarke, P. J. Talling, M. J. Cartigny, and D. Pratomo, 2016, Preconditioning and triggering of offshore slope failures and turbidity currents revealed by most detailed monitoring yet at a fjord-head delta: Earth and Planetary Science Letters, v. 450, p. 208-220.

Clare, M. A., P. J. Talling, P. Challenor, G. Malgesini, and J. Hunt, 2014, Distal turbidites reveal a common distribution for large (> 0.1 km3) submarine landslide recurrence: Geology, v. 42, p. 263-266.

Coussens, M., D. Wall‐Palmer, P. J. Talling, S. F. Watt, M. Cassidy, M. Jutzeler, M. A. Clare, J. E. Hunt, M. Manga, and T. M. Gernon, 2016, The relationship between eruptive activity, flank collapse, and sea level at volcanic islands: A long‐term (> 1 Ma) record offshore Montserrat, Lesser Antilles: Geochemistry, Geophysics, Geosystems, v. 17, p. 2591-2611.

Diegel, F. A., J. Karlo, D. Schuster, R. Shoup, and P. Tauvers, 1995, Cenozoic structural evolution and tectono-stratigraphic framework of the northern Gulf Coast continental margin.

Dott Jr, R., 1963, Dynamics of subaqueous gravity depositional processes: AAPG Bulletin, v. 47, p. 104-128.

Doughty-Jones, G., L. Lonergan, M. Mayall, and S. Dee, 2019, The role of structural growth in controlling the facies and distribution of mass transport deposits in a deep-water salt minibasin: Marine and Petroleum Geology, v. 104, p. 106-124.

Dugan, B., and P. B. Flemings, 2000, Overpressure and fluid flow in the New Jersey continental slope: Implications for slope failure and cold seeps: Science, v. 289, p. 288-291.

Franco, S. I., C. Canet, A. Iglesias, and C. Valdés-González, 2013, Seismic activity in the Gulf of Mexico. A preliminary analysis: Boletín de la Sociedad Geologíca Mexicana, v. 65, p. 447-455.

Frey Martinez, J., J. Cartwright, and B. Hall, 2005, 3D seismic interpretation of slump complexes: examples from the continental margin of Israel: Basin Research, v. 17, p. 83-108.

Frohlich, C., 1982, Seismicity of the central Gulf of Mexico: Geology, v. 10, p. 103-106.

Galloway, W. E., 2001, Cenozoic evolution of sediment accumulation in deltaic and shore-zone depositional systems, northern Gulf of Mexico Basin: Marine and Petroleum Geology, v. 18, p. 1031-1040.

Galloway, W. E., P. E. Ganey-Curry, X. Li, and R. T. Buffler, 2000, Cenozoic depositional history of the Gulf of Mexico basin: AAPG bulletin, v. 84, p. 1743-1774.

Galloway, W. E., T. L. Whiteaker, and P. Ganey-Curry, 2011, History of Cenozoic North American drainage basin evolution, sediment yield, and accumulation in the Gulf of Mexico basin: Geosphere, v. 7, p. 938-973.

Gamboa, D., T. Alves, and J. Cartwright, 2011, Distribution and characterization of failed (mega) blocks along salt ridges, southeast Brazil: Implications for vertical fluid flow on continental margins: Journal of Geophysical Research: Solid Earth, v. 116.

Gamboa, D., and T. M. Alves, 2016, Bi-modal deformation styles in confined mass-transport deposits: Examples from a salt minibasin in SE Brazil: Marine Geology, v. 379, p. 176-193.

Gangopadhyay, A., and M. K. Sen, 2008, A possible mechanism for the spatial distribution of seismicity in northern Gulf of Mexico: Geophysical Journal International, v. 175, p. 1141-1153.

Gee, M., D. Masson, A. Watts, and P. Allen, 1999, The Saharan debris£ ow: an insight into the mechanics of long runout submarine debris£ ows: Sedimentology, v. 46, p. 317-335.

Giles, K. A., and T. F. Lawton, 2002, Halokinetic sequence stratigraphy adjacent to the El Papalote diapir, northeastern Mexico: AAPG bulletin, v. 86, p. 823-840.

Giles, K. A., and M. G. Rowan, 2012, Concepts in halokinetic-sequence deformation and stratigraphy: Geological Society, London, Special Publications, v. 363, p. 7-31.

Grozic, J., 2010, Interplay between gas hydrates and submarine slope failure, Submarine mass movements and their consequences, Springer, p. 11-30.

Hampton, M. A., H. J. Lee, and J. Locat, 1996, Submarine landslides: Reviews of geophysics, v. 34, p. 33-59.

Harbitz, C. B., F. Løvholt, and H. Bungum, 2014, Submarine landslide tsunamis: how extreme and how likely?: Natural Hazards, v. 72, p. 1341-1374.

Hearon, T. E., M. G. Rowan, K. A. Giles, and W. H. Hart, 2014, Halokinetic deformation adjacent to the deepwater Auger diapir, Garden Banks 470, northern Gulf of Mexico: Testing the applicability of an outcrop-based model using subsurface data: Interpretation, v. 2, p. SM57-SM76.

Hill, A., J. Southgate, P. Fish, and S. Thomas, 2011, Deepwater Angola part I: Geohazard mitigation: Frontiers in Offshore Geotechnics II, p. 209-214.

Hjelstuen, B. O., O. Eldholm, and J. I. Faleide, 2007, Recurrent Pleistocene mega-failures on the SW Barents Sea margin: Earth and Planetary Science Letters, v. 258, p. 605-618.

Hudec, M. R., M. P. Jackson, and D. D. Schultz-Ela, 2009, The paradox of minibasin subsidence into salt: Clues to the evolution of crustal basins: Geological Society of America Bulletin, v. 121, p. 201-221.

Hühnerbach, V., and D. Masson, 2004, Landslides in the North Atlantic and its adjacent seas: an analysis of their morphology, setting and behaviour: Marine Geology, v. 213, p. 343-362.

Imbrie, J., J. D. Hays, D. G. Martinson, A. McIntyre, A. C. Mix, J. J. Morley, N. G. Pisias, W. L. Prell, and N. J. Shackleton, 1984, The orbital theory of Pleistocene climate: support from a revised chronology of the marine d18O record.

Jackson, C. A.-L., O. B. Duffy, N. Fernandez, T. Dooley, M. Hudec, M. Jackson, and G. Burg, 2019, The Stratigraphic Record of Minibasin Subsidence.

Kioka, A., T. Schwestermann, J. Moernaut, K. Ikehara, T. Kanamatsu, C. McHugh, C. dos Santos Ferreira, G. Wiemer, N. Haghipour, and A. Kopf, 2019, Megathrust earthquake drives drastic organic carbon supply to the hadal trench: Scientific reports, v. 9, p. 1553.

Kneller, E. A., and C. A. Johnson, 2011, Plate kinematics of the Gulf of Mexico based on integrated observations from the Central and South Atlantic.

Kvalstad, T. J., L. Andresen, C. F. Forsberg, K. Berg, P. Bryn, and M. Wangen, 2005, The Storegga slide: evaluation of triggering sources and slide mechanics: Marine and Petroleum Geology, v. 22, p. 245-256.

Lastras, G., F. V. De Blasio, M. Canals, and A. Elverhøi, 2005, Conceptual and numerical modeling of the BIG'95 debris flow, western Mediterranean Sea: Journal of Sedimentary Research, v. 75, p. 784-797.

Li, W., T. M. Alves, S. Wu, D. Völker, F. Zhao, L. Mi, and A. Kopf, 2015, Recurrent slope failure and submarine channel incision as key factors controlling reservoir potential in the South China Sea (Qiongdongnan Basin, South Hainan Island): Marine and Petroleum Geology, v. 64, p. 17-30.

Locat, J., and H. J. Lee, 2002, Submarine landslides: advances and challenges: Canadian Geotechnical Journal, v. 39, p. 193-212.

MacDonald, I., N. Guinasso Jr, R. Sassen, J. Brooks, L. Lee, and K. Scott, 1994, Gas hydrate that breaches the sea floor on the continental slope of the Gulf of Mexico: Geology, v. 22, p. 699-702.

Madof, A. S., N. Christie-Blick, and M. H. Anders, 2009, Stratigraphic controls on a salt-withdrawal intraslope minibasin, north-central Green Canyon, Gulf of Mexico: Implications for misinterpreting sea level change: AAPG bulletin, v. 93, p. 535-561.

Madof, A. S., N. Christie-Blick, M. H. Anders, and L. A. Febo, 2017, Unreciprocated sedimentation along a mud-dominated continental margin, Gulf of Mexico, USA: Implications for sequence stratigraphy in muddy settings devoid of depositional sequences: Marine and Petroleum Geology, v. 80, p. 492-516.

Mallarino, G., R. T. Beaubouef, A. W. Droxler, V. Abreu, and L. Labeyrie, 2006, Sea level influence on the nature and timing of a minibasin sedimentary fill (northwestern slope of the Gulf of Mexico): AAPG bulletin, v. 90, p. 1089-1119.

Maslin, M., N. Mikkelsen, C. Vilela, and B. Haq, 1998, Sea-level–and gas-hydrate–controlled catastrophic sediment failures of the Amazon Fan: Geology, v. 26, p. 1107-1110.

Masson, D., C. Harbitz, R. Wynn, G. Pedersen, and F. Løvholt, 2006, Submarine landslides: processes, triggers and hazard prediction: Philosophical Transactions of the Royal Society A: Mathematical, Physical and Engineering Sciences, v. 364, p. 2009-2039.

Masson, D., R. Wynn, and P. Talling, 2010, Large landslides on passive continental margins: processes, hypotheses and outstanding questions, Submarine mass movements and their consequences, Springer, p. 153-165.

McHugh, C. M., J. E. Damuth, and G. S. Mountain, 2002, Cenozoic mass-transport facies and their correlation with relative sea-level change, New Jersey continental margin: Marine Geology, v. 184, p. 295-334.

Mienert, J., M. Vanneste, S. Bünz, K. Andreassen, H. Haflidason, and H. P. Sejrup, 2005, Ocean warming and gas hydrate stability on the mid-Norwegian margin at the Storegga Slide: Marine and Petroleum Geology, v. 22, p. 233-244.

Milkov, A. V., and R. Sassen, 2001, Estimate of gas hydrate resource, northwestern Gulf of Mexico continental slope: Marine Geology, v. 179, p. 71-83.

Molnar, P., 2004, Late Cenozoic increase in accumulation rates of terrestrial sediment: How might climate change have affected erosion rates?: Annu. Rev. Earth Planet. Sci., v. 32, p. 67-89.

Moscardelli, L., and L. Wood, 2008, New classification system for mass transport complexes in offshore Trinidad: Basin Research, v. 20, p. 73-98.

Moscardelli, L., L. Wood, and P. Mann, 2006, Mass-transport complexes and associated processes in the offshore area of Trinidad and Venezuela: AAPG bulletin, v. 90, p. 1059-1088.

Nardin, T. R., F. Hein, D. S. Gorsline, and B. Edwards, 1979, A review of mass movement processes sediment and acoustic characteristics, and contrasts in slope and base-of-slope systems versus canyon-fan-basin floor systems.

Nisbet, E. G., and D. J. Piper, 1998, Giant submarine landslides: Nature, v. 392, p. 329-330.

O'loughlin, K. F., and J. F. Lander, 2003, Caribbean tsunamis: a 500-year history from 1498-1998, v. 20, Springer Science & Business Media.

Omosanya, K. O., and T. M. Alves, 2013, A 3-dimensional seismic method to assess the provenance of Mass-Transport Deposits (MTDs) on salt-rich continental slopes (Espírito Santo Basin, SE Brazil): Marine and Petroleum Geology, v. 44, p. 223-239.

Ortiz‐Karpf, A., D. M. Hodgson, C. A. L. Jackson, and W. D. McCaffrey, 2016, Mass‐Transport Complexes as Markers of Deep‐Water Fold‐and‐Thrust Belt Evolution: Insights from the Southern Magdalena Fan, Offshore Colombia: Basin Research.

Owen, M., S. Day, and M. Maslin, 2007, Late Pleistocene submarine mass movements: occurrence and causes: Quaternary Science Reviews, v. 26, p. 958-978.

Perov, G., and J. P. Bhattacharya, 2011, Pleistocene shelf-margin delta: Intradeltaic deformation and sediment bypass, northern Gulf of Mexico: AAPG bulletin, v. 95, p. 1617-1641.

Pindell, J., and J. F. Dewey, 1982, Permo‐Triassic reconstruction of western Pangea and the evolution of the Gulf of Mexico/Caribbean region: Tectonics, v. 1, p. 179-211.

Pope, E., P. Talling, M. Urlaub, J. Hunt, M. Clare, and P. Challenor, 2015, Are large submarine landslides temporally random or do uncertainties in available age constraints make it impossible to tell?: Marine Geology, v. 369, p. 19-33.

Posamentier, H., M. Jervey, and P. Vail, 1988, Eustatic controls on clastic deposition I—conceptual framework.

Posamentier, H., and R. Walker, 2006, Deep-water turbidites and submarine fans. Facies Models Revisited: Special Publication-Society for Sedimentary Geology, v. 84, p. 399-520.

Posamentier, H. W., and V. Kolla, 2003, Seismic geomorphology and stratigraphy of depositional elements in deep-water settings: Journal of Sedimentary Research, v. 73, p. 367-388.

Prather, B., 2000, Calibration and visualization of depositional process models for above-grade slopes: a case study from the Gulf of Mexico: Marine and Petroleum Geology, v. 17, p. 619-638.

Prather, B. E., J. R. Booth, G. S. Steffens, and P. A. Craig, 1998, Classification, lithologic calibration, and stratigraphic succession of seismic facies of intraslope basins, deep-water Gulf of Mexico: AAPG bulletin, v. 82, p. 701-728.

Prather, B. E., C. Pirmez, C. D. Winker, M. Deptuck, and D. Mohrig, 2012, Stratigraphy of linked intraslope basins: Brazos-Trinity system western Gulf of Mexico: Application of the principles of seismic geomorphology to continental-slope and base-of-slope systems: Case studies from seafloor and near-seafloor analogues: SEPM, Special Publication, v. 99, p. 83-109.

Rittenour, T. M., M. D. Blum, and R. J. Goble, 2007, Fluvial evolution of the lower Mississippi River valley during the last 100 ky glacial cycle: Response to glaciation and sea-level change: GSA Bulletin, v. 119, p. 586-608.

Roesink, J. G., P. Weimer, and R. Bouroullec, 2004, Sequence stratigraphy of Miocene to Pleistocene sediments of east-central Mississippi canyon, northern Gulf of Mexico.

Rowan, M. G., T. F. Lawton, K. A. Giles, and R. A. Ratliff, 2003, Near-salt deformation in La Popa basin, Mexico, and the northern Gulf of Mexico: A general model for passive diapirism: AAPG bulletin, v. 87, p. 733-756.

Rowan, M. G., and P. Weimer, 1998, Salt-sediment interaction, northern Green Canyon and Ewing bank (offshore Louisiana), northern Gulf of Mexico: AAPG bulletin, v. 82, p. 1055-1082.

Salazar, J. A., J. H. Knapp, C. C. Knapp, and D. R. Pyles, 2014, Salt tectonics and Pliocene stratigraphic framework at MC-118, Gulf of Mexico: An integrated approach with application to deep-water confined structures in salt basins: Marine and Petroleum Geology, v. 50, p. 51-67.

Salvador, A., 1987, Late Triassic-Jurassic paleogeography and origin of Gulf of Mexico basin: AAPG Bulletin, v. 71, p. 419-451.

Sawyer, D. E., P. B. Flemings, B. Dugan, and J. T. Germaine, 2009, Retrogressive failures recorded in mass transport deposits in the Ursa Basin, Northern Gulf of Mexico: Journal of Geophysical Research: Solid Earth, v. 114.

Sawyer, D. E., P. B. Flemings, R. C. Shipp, and C. D. Winker, 2007, Seismic geomorphology, lithology, and evolution of the late Pleistocene Mars-Ursa turbidite region, Mississippi Canyon area, northern Gulf of Mexico: AAPG bulletin, v. 91, p. 215-234.

Shipp, R. C., 2004, Physical Characteristics and Impact of Mass Transport Complexes on Deepwater Jetted Conductors and Suction Anchor Piles.

Siesser, W. G., 1998, Calcareous nannofossil genus Scyphosphaera: structure, taxonomy, biostratigraphy, and phylogeny: Micropaleontology, p. 351-384.

Sincavage, R., P. Weimer, and R. Bouroullec, 2004, Sequence Stratigraphy of Upper-Miocene to Pleistocene Sediments of Southwestern Mississippi Canyon and Northwestern Atwater Valley, Northern Gulf of Mexico.

Smith, D., S. Harrison, and J. T. Jordan, 2013, Sea level rise and submarine mass failures on open continental margins: Quaternary Science Reviews, v. 82, p. 93-103.

Strout, J. M., and T. I. Tjelta, 2005, In situ pore pressures: What is their significance and how can they be reliably measured?: Marine and Petroleum Geology, v. 22, p. 275-285.

Sydow, J., J. Finneran, A. P. Bowman, H. Roberts, N. Rosen, R. Fillon, and J. Anderson, 2003, Stacked shelf-edge delta reservoirs of the Columbus Basin, Trinidad, West Indies: Shelf-Margin Deltas and Linked Downslope Petroleum Systems, p. 441-465.

Sylvester, Z., A. Cantelli, and C. Pirmez, 2015, Stratigraphic evolution of intraslope minibasins: Insights from surface-based model: AAPG Bulletin, v. 99, p. 1099-1129.

Talling, P. J., L. A. Amy, and R. B. Wynn, 2007, New insight into the evolution of large ‐ volume turbidity currents: comparison of turbidite shape and previous modelling results: Sedimentology, v. 54, p. 737-769.

Talling, P. J., M. L. CLARE, M. Urlaub, E. Pope, J. E. Hunt, and S. F. Watt, 2014, Large submarine landslides on continental slopes: geohazards, methane release, and climate change: Oceanography, v. 27, p. 32-45.

Tripsanas, E. K., W. R. Bryant, and B. A. Phaneuf, 2004, Slope-instability processes caused by salt movements in a complex deep-water environment, Bryant Canyon area, northwest Gulf of Mexico: AAPG bulletin, v. 88, p. 801-823.

Twichell, D. C., J. D. Chaytor, S. Uri, and B. Buczkowski, 2009, Morphology of late Quaternary submarine landslides along the US Atlantic continental margin: Marine Geology, v. 264, p. 4-15.

Urlaub, M., P. J. Talling, and D. G. Masson, 2013, Timing and frequency of large submarine landslides: implications for understanding triggers and future geohazard: Quaternary Science Reviews, v. 72, p. 63-82.

Vail, P. R., R. Mitchum Jr, and S. Thompson III, 1977, Seismic Stratigraphy and Global Changes of Sea Level: Part 4. Global Cycles of Relative Changes of Sea Level.: Section 2. Application of Seismic Reflection Configuration to Stratigraphic Interpretation.

Waterman, A., R. Weber, B. Brace, J. Edmunds, R. Fillon, R. George, Y. Lu, N. Myers, B. Parker, and T. Reilly, 2015, Biostratigraphic chart—Gulf Basin, USA: Quaternary and Neogene.

Weaver, P. P., R. B. Wynn, N. H. Kenyon, and J. Evans, 2000, Continental margin sedimentation, with special reference to the north ‐ east Atlantic margin: Sedimentology, v. 47, p. 239-256.

Weimer, P., and C. Shipp, 2004, Mass transport complex: musing on past uses and suggestions for future directions: Offshore Technology Conference.

Winker, C. D., and J. R. Booth, 2000, Sedimentary dynamics of the salt-dominated continental slope, Gulf of Mexico: integration of observations from the seafloor, near-surface, and deep subsurface: GCSSEPM Foundation 20th Annual Research Conference, Deep-Water Reservoirs of the World, p. 1059-1086.

Witrock, R., A. Friedmann, J. Galluzzo, L. Nixon, P. Post, and K. Ross, 2003, Biostratigraphic chart of the Gulf of Mexico offshore region: Jurassic to Quaternary, US Department of the Interior, Minerals Management Service, New Orleans.

Wu, N., C. A. Jackson, H. Johnson, and D. M. Hodgson, 2019, Lithological, petrophysical and seal properties of mass-transport complexes (MTCs), northern Gulf of Mexico: EarthArXiv. February, v. 19.

Yeakley, J. A., A. Shakoor, and W. Johnson, 2019, Influence of Salt Tectonics On Fault Displacements and Submarine Slope Failures from Algeria To Sardinia: Environmental & Engineering Geoscience, p. 1-13.

Young, J. R., 1998, Neogene: Calcareous nannofossil biostratigraphy, p. 225-265.

Figure 1

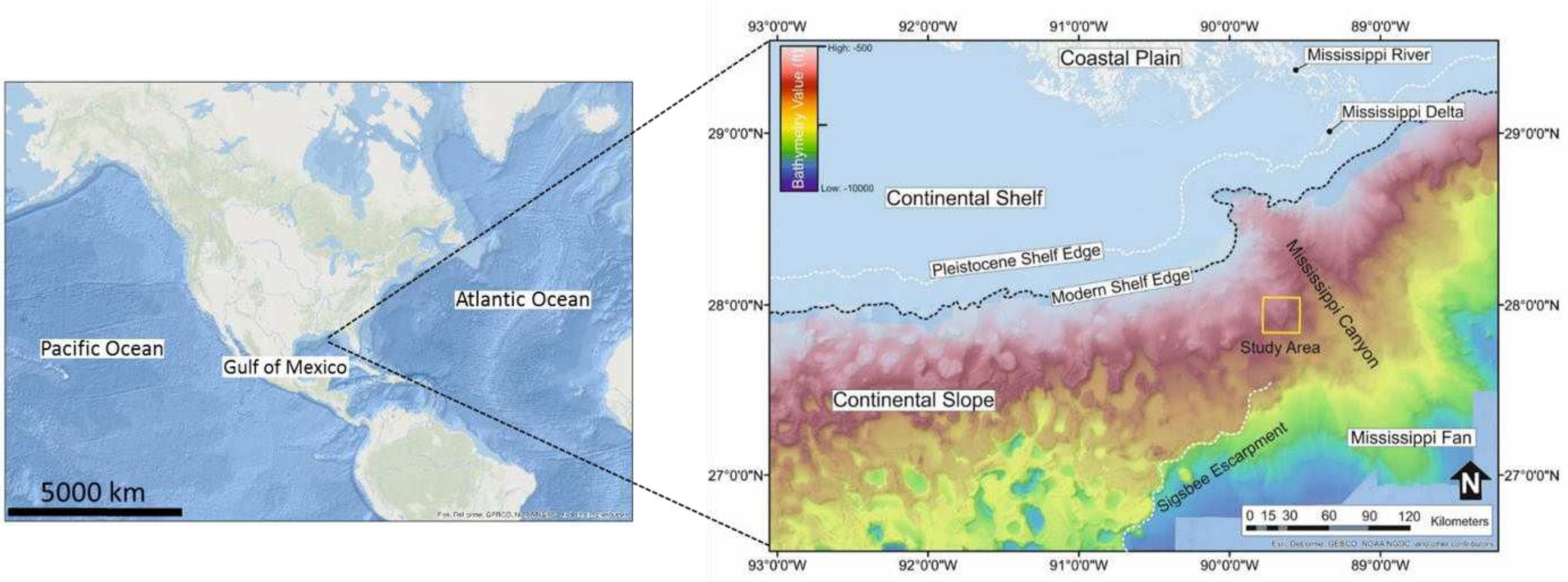

Pacific Ocean
Atlantic Ocean
Gulf of Mexico
5000 km
93°0'0"W
92°0'0"W
91°0'0"W
90°0'0"W
89°0'0"W
29°0'0"N
28°0'0"N
27°0'0"N
High: -500
Bathymetry Value (ft)
Low: -10000
Coastal Plain
Mississippi River
Mississippi Delta
Continental Shelf
Pleistocene Shelf Edge
Modern Shelf Edge
Mississippi Canyon
Study Area
Continental Slope
Sigsbee Escarpment
Mississippi Fan
N
0 15 30 60 90 120 Kilometers

Figure 2

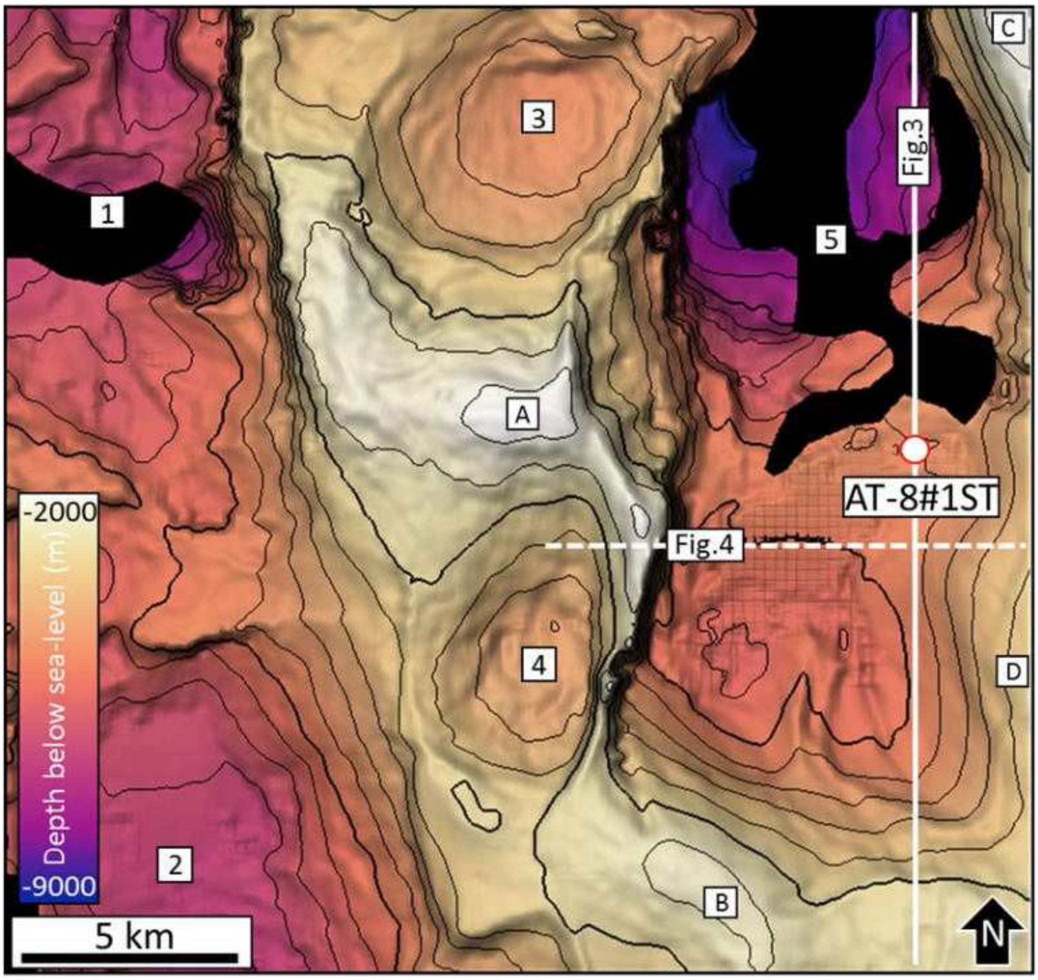

C
3
Fig.3
1
5
A
AT-8#1ST
-2000
Depth below sea-level (m)
Fig.4
4
D
-9000
2
B
5 km
N

Figure 3a

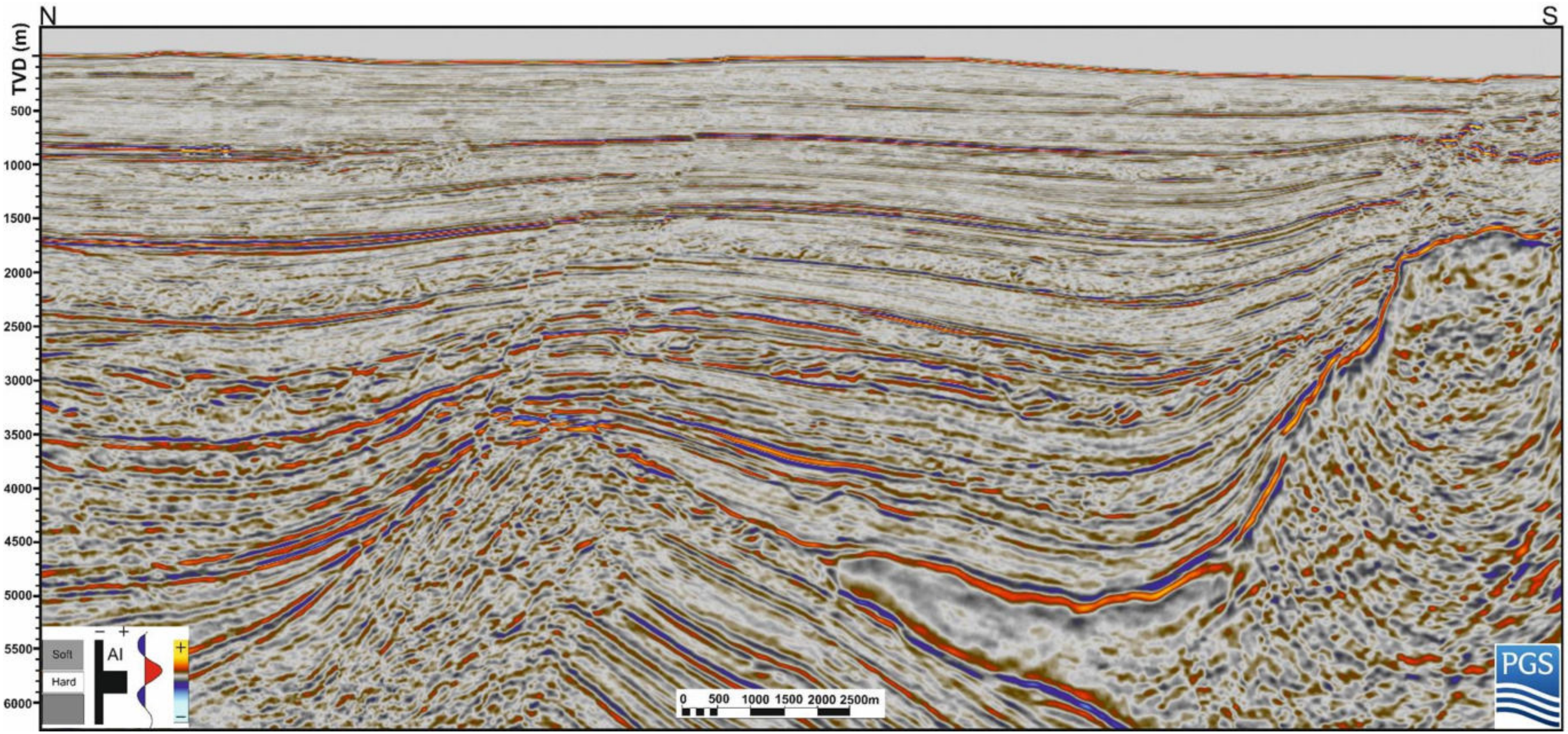

N
S
TVD (m)
500
1000
1500
2000
2500
3000
3500
4000
4500
5000
5500
6000
Soft
Hard
AI
0 500 1000 1500 2000 2500m
PGS

Figure 3b

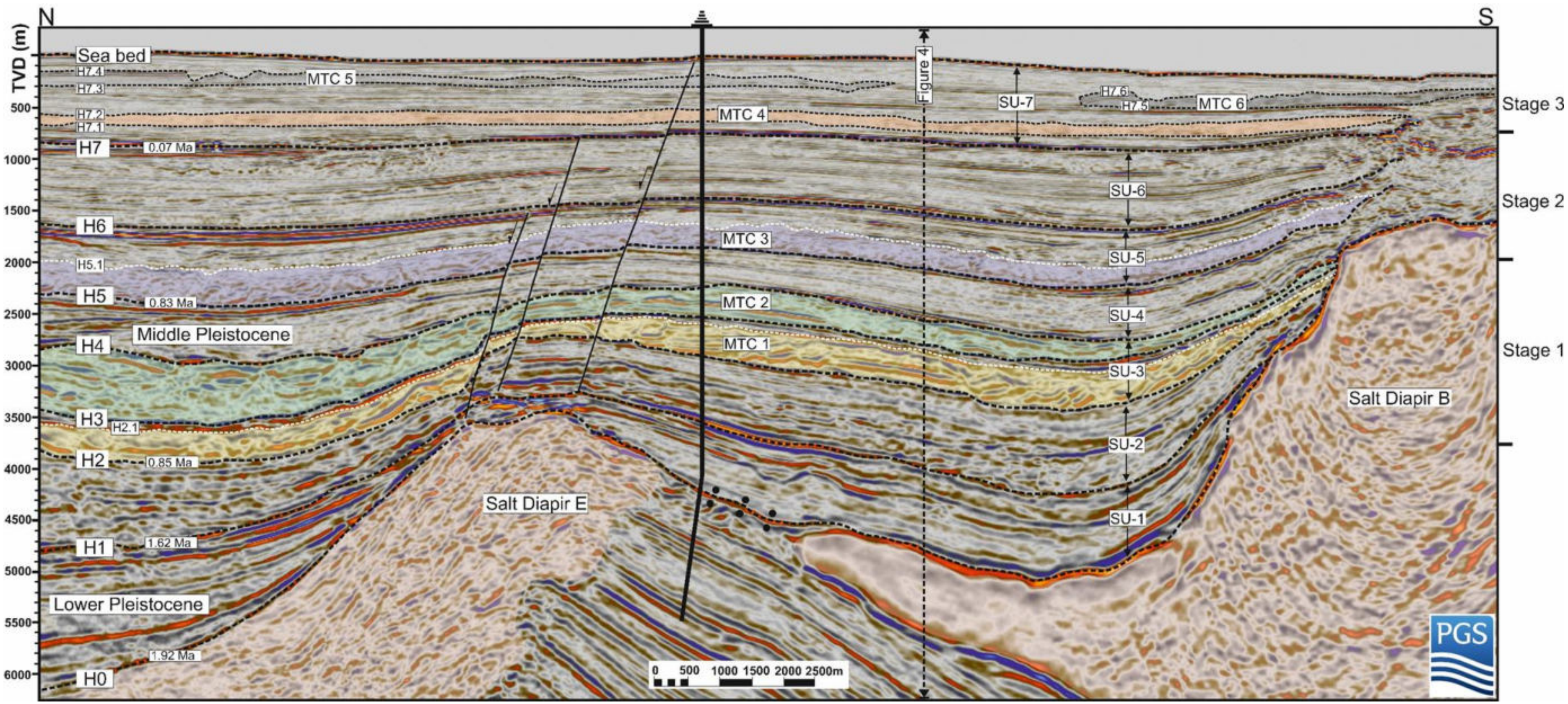
N
S
TVD (m)
500
1000
1500
2000
2500
3000
3500
4000
4500
5000
5500
6000
Sea bed
H7.4
H7.3
H7.2
H7.1
H7
0.07 Ma
H6
H5.1
H5
0.83 Ma
H4
Middle Pleistocene
H3
H2.1
H2
0.85 Ma
H1
1.62 Ma
Lower Pleistocene
1.92 Ma
H0
MTC 5
MTC 4
MTC 3
MTC 2
MTC 1
Figure 4
SU-7
SU-6
SU-5
SU-4
SU-3
SU-2
SU-1
H7.6
H7.5
MTC 6
Stage 3
Stage 2
Stage 1
Salt Diapir E
Salt Diapir B
0 500 1000 1500 2000 2500m
PGS

Figure 4a

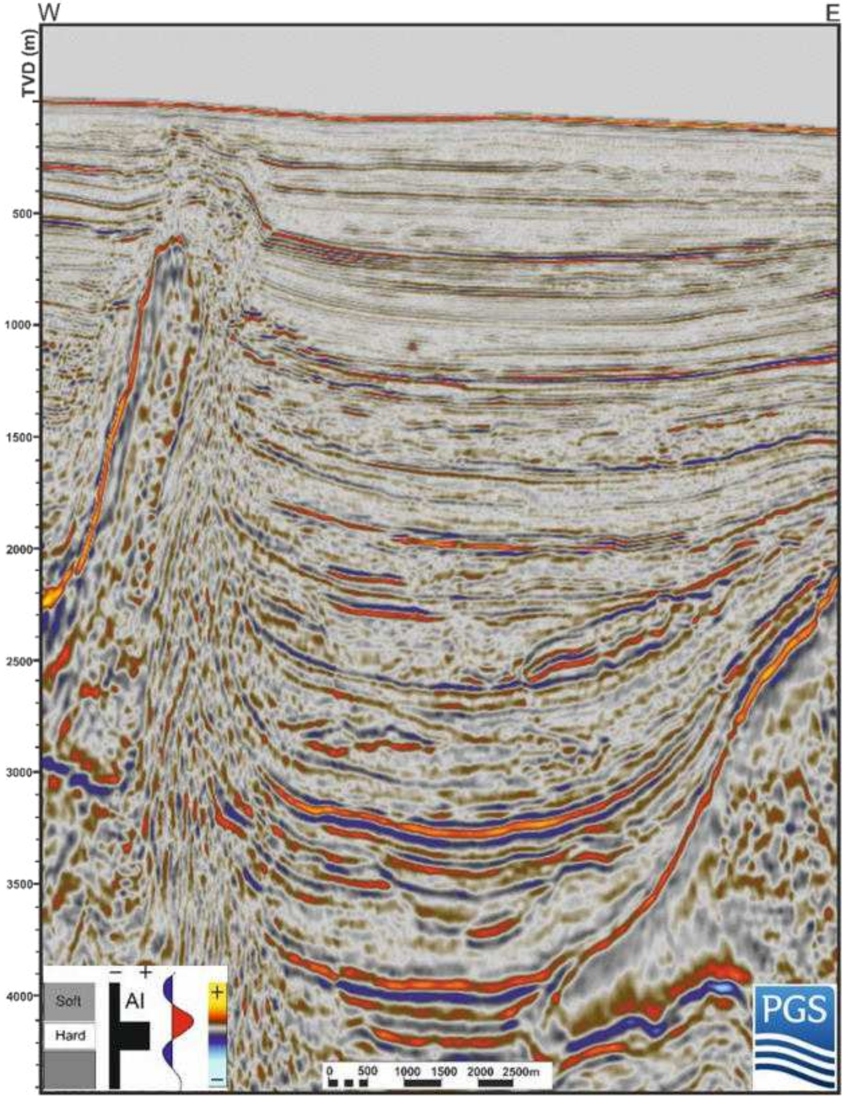

Figure 4b

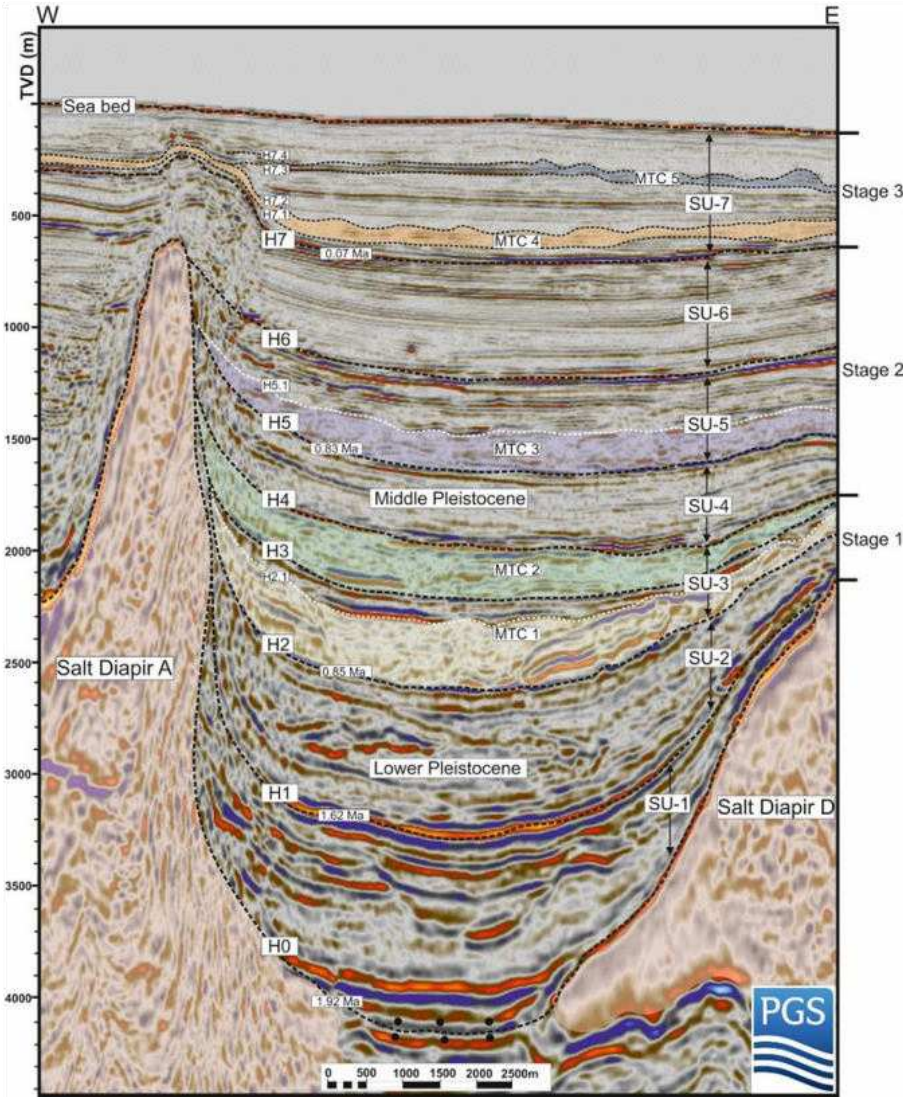

Figure 5

Seismic facies template

Types		Seismic sections / GR / Sonic / Lithology / Schematic facies geometries	Seismic facies	Log facies	Lithology	Depositional element
Stratified facies	SFs1	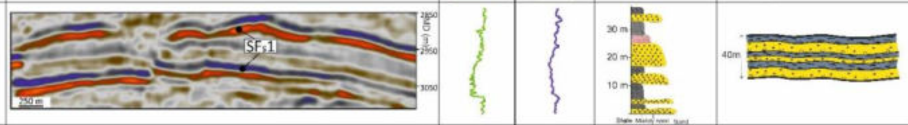	Fair continuity, parallel, high amplitude seismic reflections, with slightly inclined, non-erosive planar base and top surface.	Fining upward trend with low GR response at the base and high GR response at the top.	Sandstone rich at the bottom and grading upward into mudstone rich deposits at the top.	Heterogeneous gravity flow deposit: •Levees • Lobes •Channel systems.
	SFs2	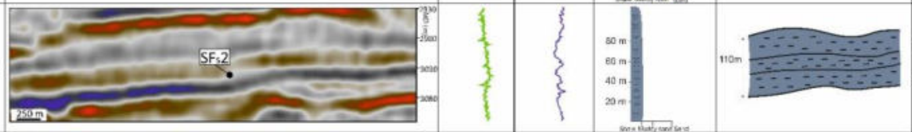	Fair continuity, parallel, low- to medium amplitude seismic reflections, with flat base and top surfaces.	Constantly serrated high GR response from bottom to top.	Mudstone rich deposits from base to top.	Slope.
	SFs3	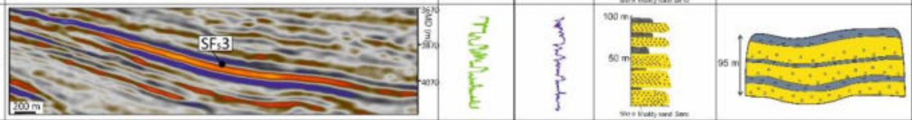	•Fair continuity, high-amplitude seismic reflections, with non-erosive, oblique top and base surfaces.	•Box-shaped GR response at base and middle, bell-shaped with upward fining GR response at the top.	Sandstone rich deposit dominant interbedded with mudstone deposits.	Lobes.
Chaotic facies	SFc1	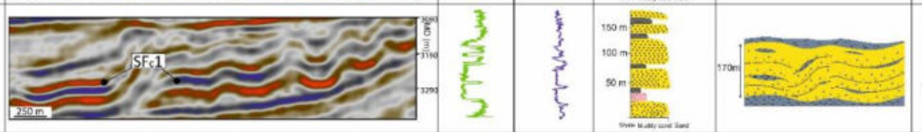	Locally disorganised, faulted and folded, high amplitude seismic reflections, with a tabular external form.	Bell-shaped GR response with a fining upward trend near the bottom, and a set of box-shaped low GR response at middle and top.	Mudstone-rich deposit at the bottom, sandstone-rich deposits interbedded with thinly bedded mudstone at the middle and upper parts.	MTCs containing large sandstone-rich blocks.
	SFc2	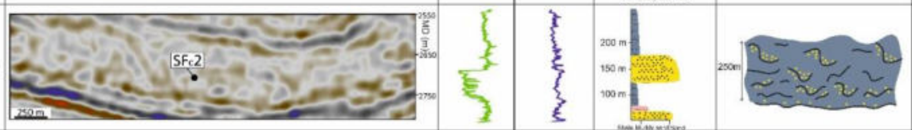	Mixture of low to medium amplitude seismic reflections with highly chaotic internal reflection pattern.	Serrated, overall high GR response that locally contains sharp-based, box-shaped, low GR intervals from base to top.	Mudstone-rich deposit interbedded with sandstone rich blocks.	Mudstone dominated MTCsSubordinate sandstones blocks (30-60 m).
	SFc3	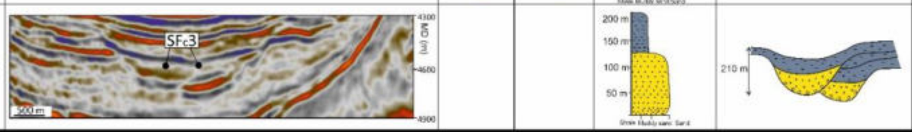	Chaotic, medium-high amplitude seismic reflections, 'bowl' shaped external form with an erosional base.		Sandstone rich deposits.	Sandstone dominant slope channel.

Figure 6

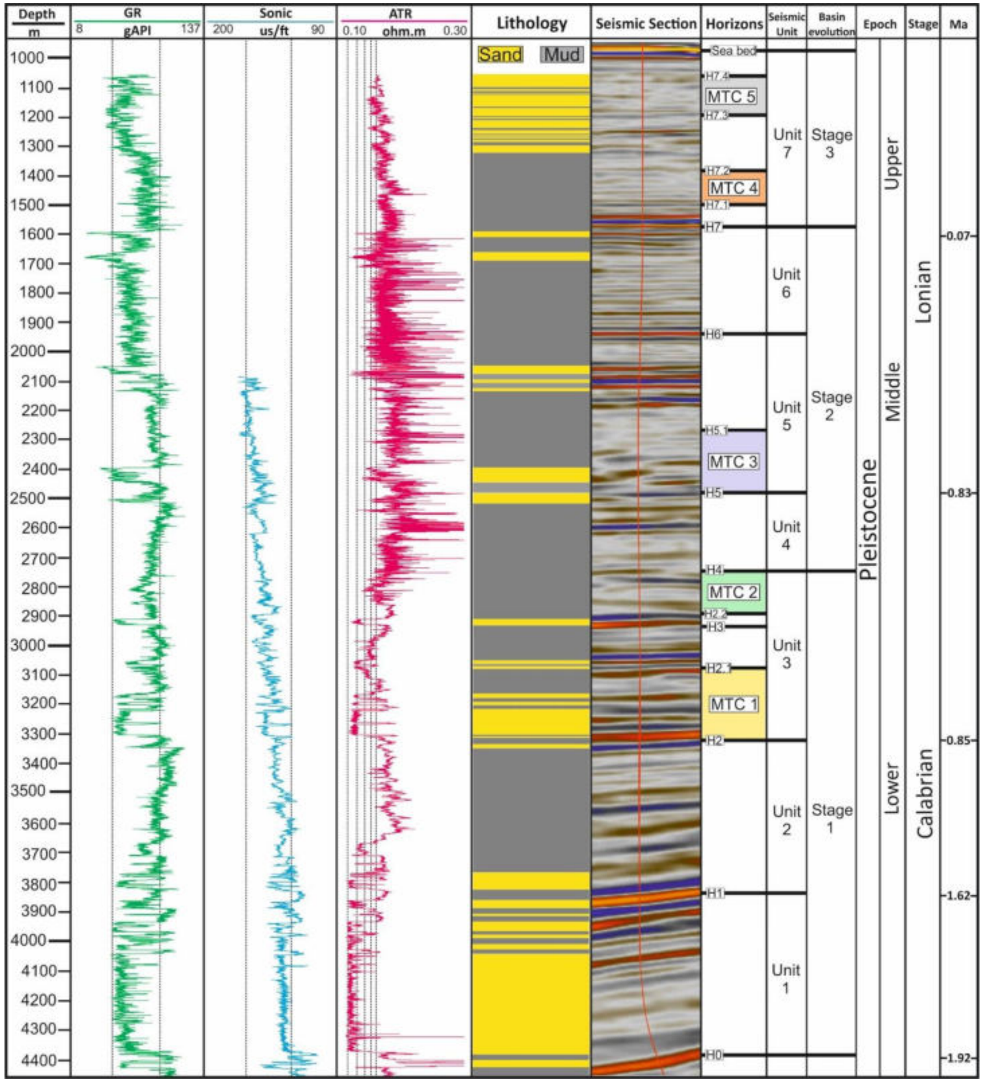

Depth m
GR 8 gAPI 137
Sonic 200 us/ft 90
ATR 0.10 ohm.m 0.30
Lithology
Sand
Mud
Seismic Section
Horizons
Seismic Unit
Basin evolution
Epoch
Stage
Ma
1000
1100
1200
1300
1400
1500
1600
1700
1800
1900
2000
2100
2200
2300
2400
2500
2600
2700
2800
2900
3000
3100
3200
3300
3400
3500
3600
3700
3800
3900
4000
4100
4200
4300
4400
Sea bed
H7.4
MTC 5
H7.3
H7.2
MTC 4
H7.1
H7
H6
H5.1
MTC 3
H5
H4
MTC 2
H2.2
H3
H2.1
MTC 1
H2
H1
H0
Unit 7
Unit 6
Unit 5
Unit 4
Unit 3
Unit 2
Unit 1
Stage 3
Stage 2
Stage 1
Pleistocene
Upper
Middle
Lower
Lonian
Calabrian
0.07
0.83
0.85
1.62
1.92

Figure 7a

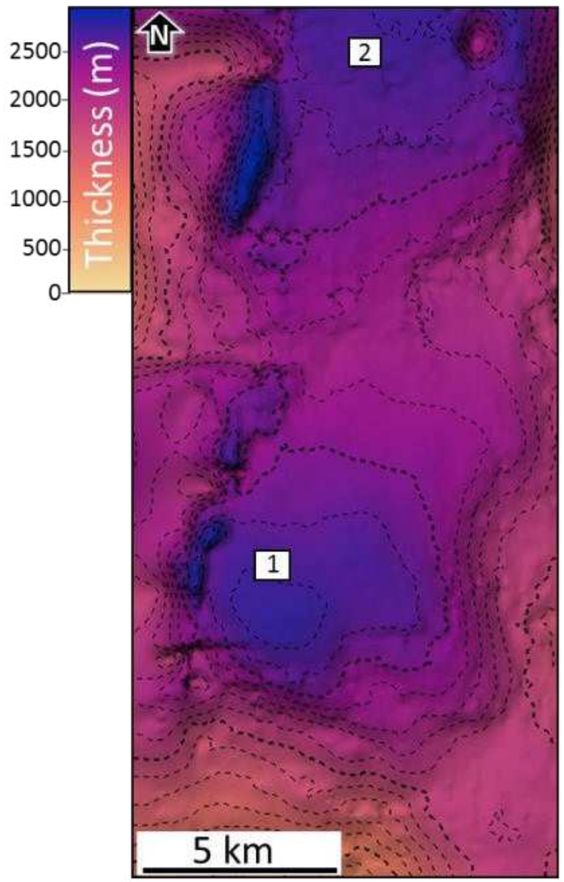

Figure 7b

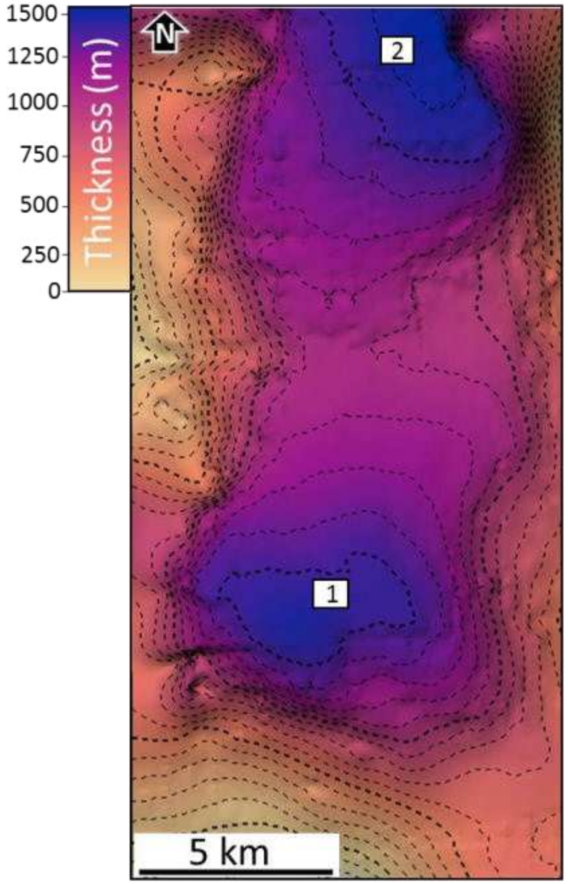

Figure 7c

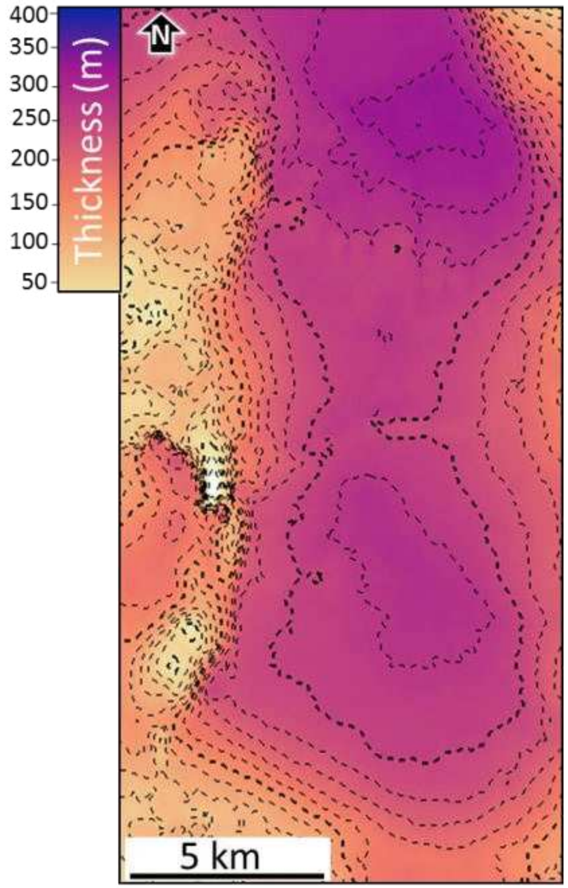

Figure 8a

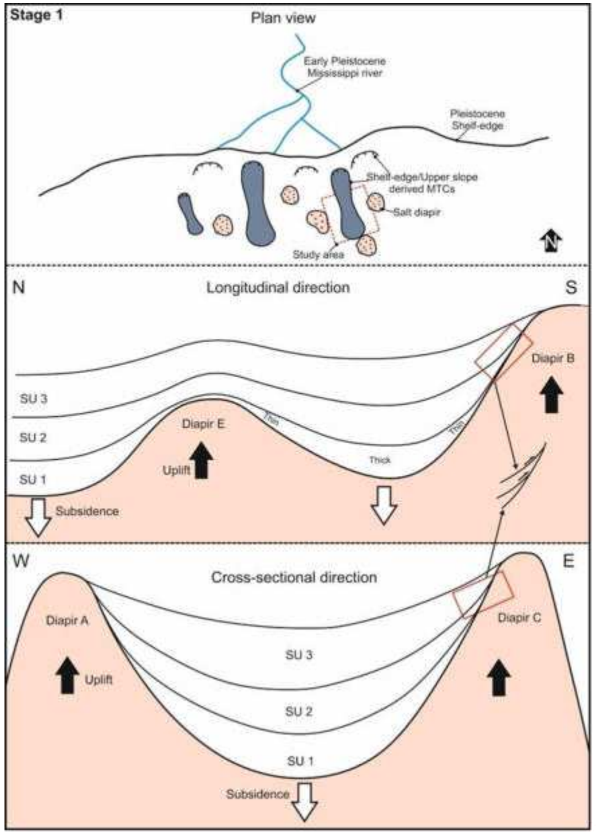

Figure 8b

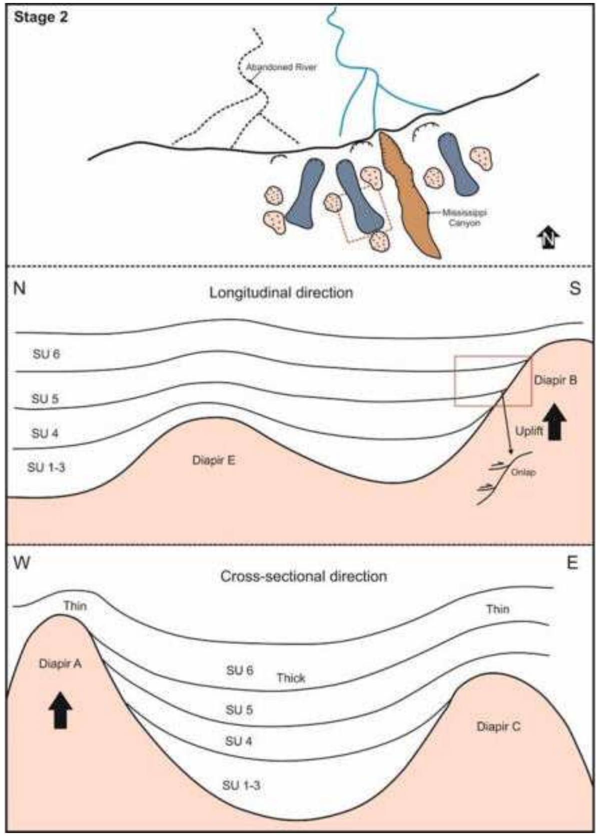

Figure 8c

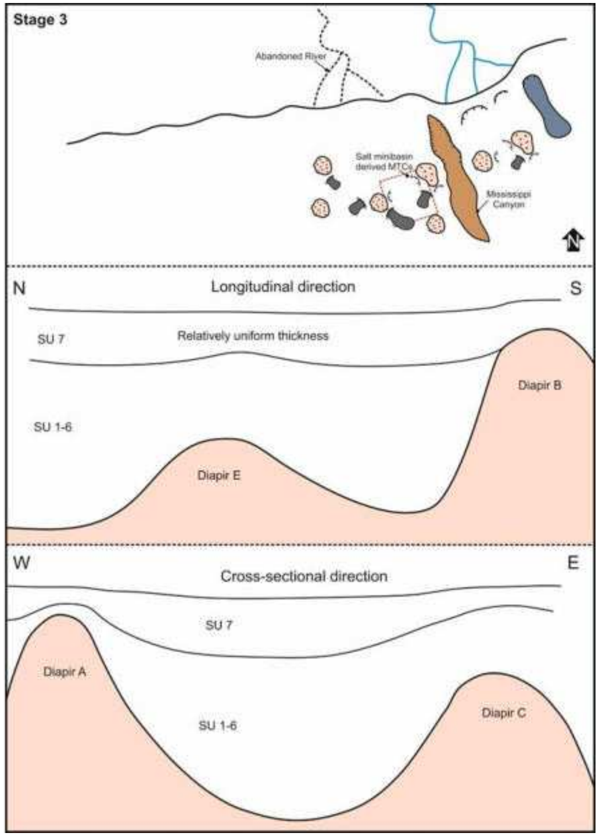

Figure 9

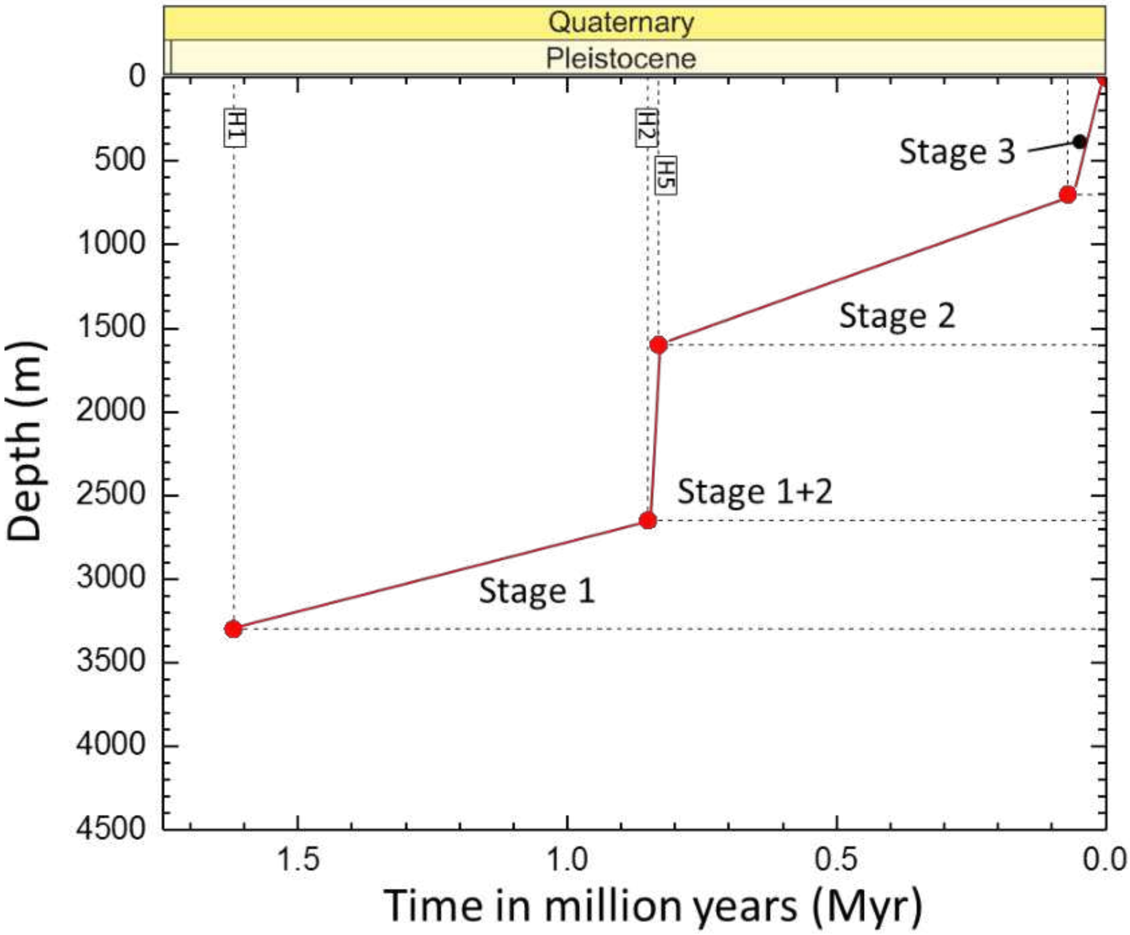
Quaternary
Pleistocene
H1
H2
H5
Stage 3
Stage 2
Stage 1+2
Stage 1
Depth (m)
0
500
1000
1500
2000
2500
3000
3500
4000
4500
1.5
1.0
0.5
0.0
Time in million years (Myr)

Figure 10a

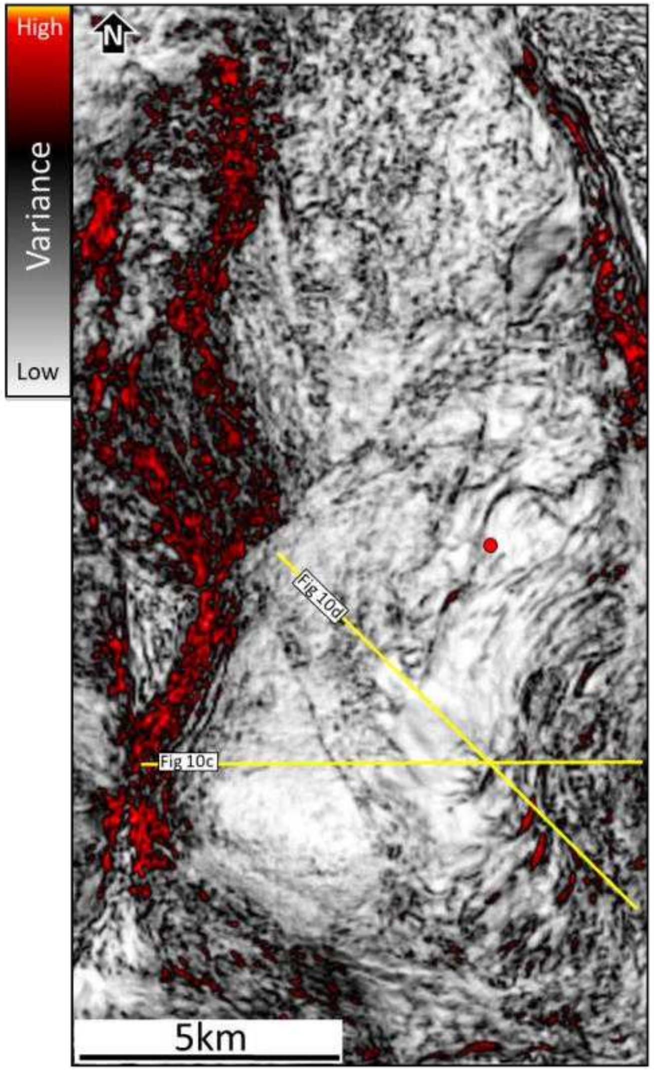

Figure 10b

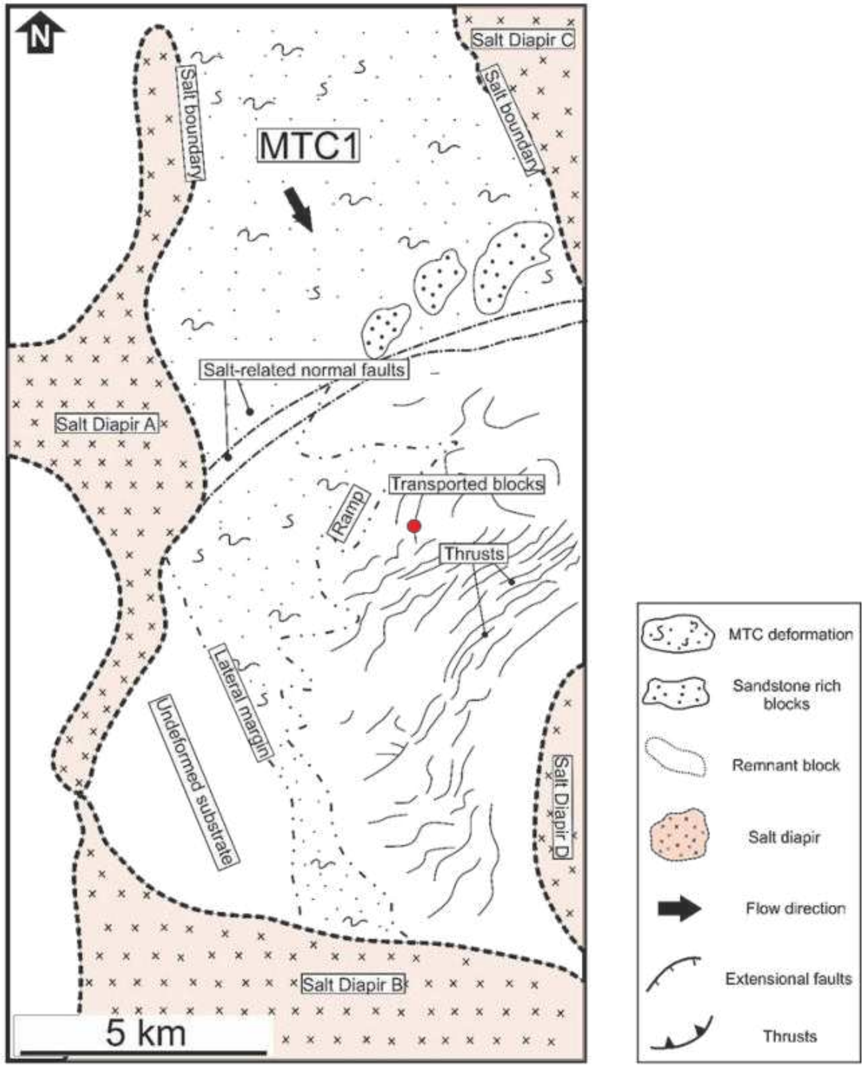

Figure 10c

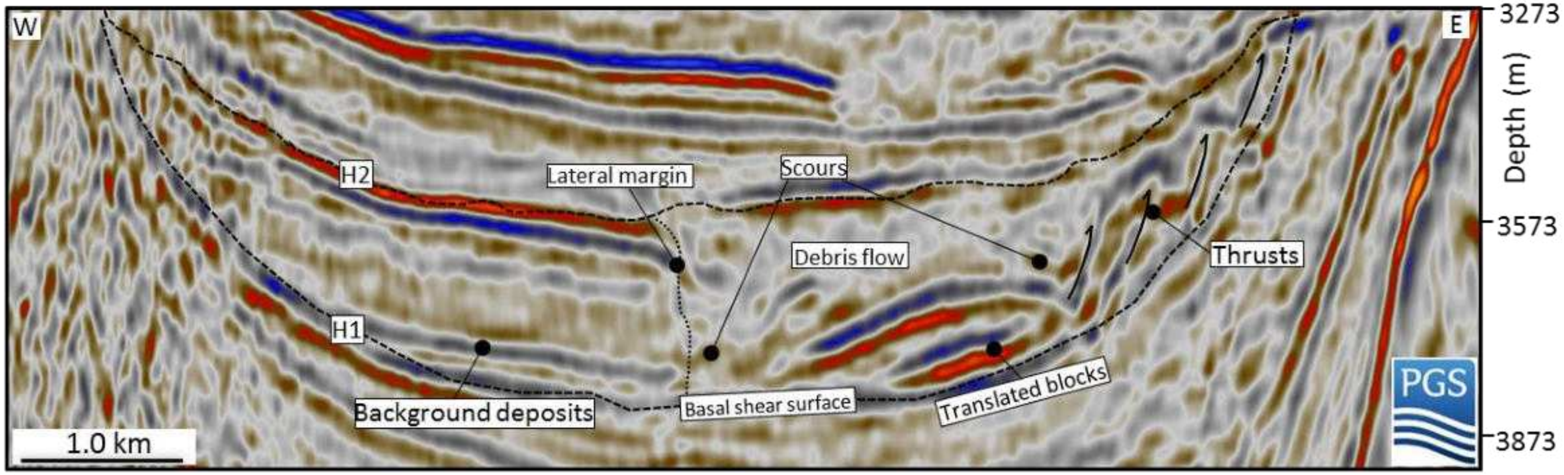

Figure 10d

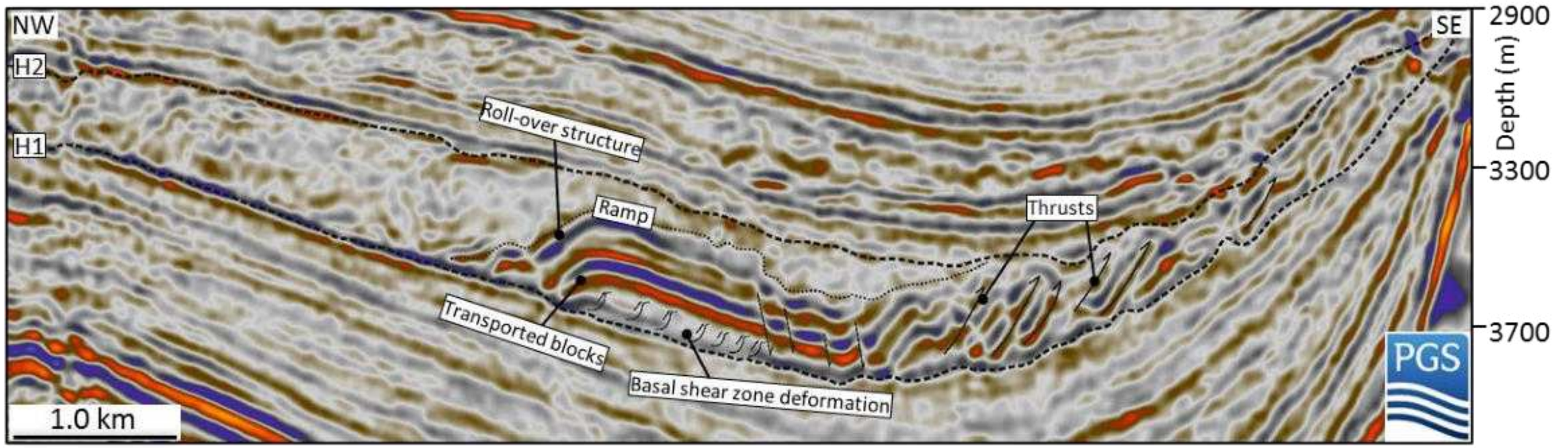

Figure 11a

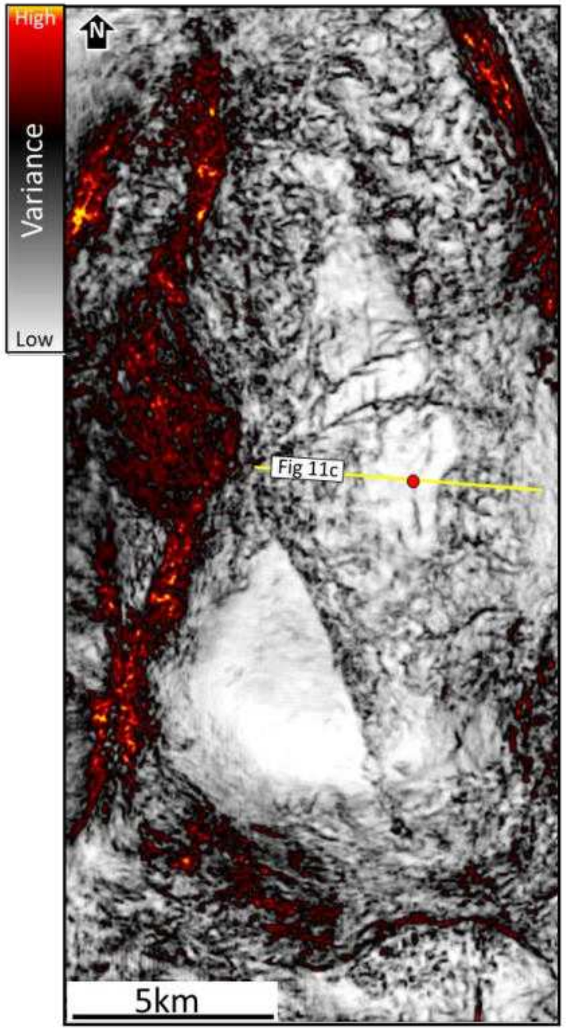

Figure 11b

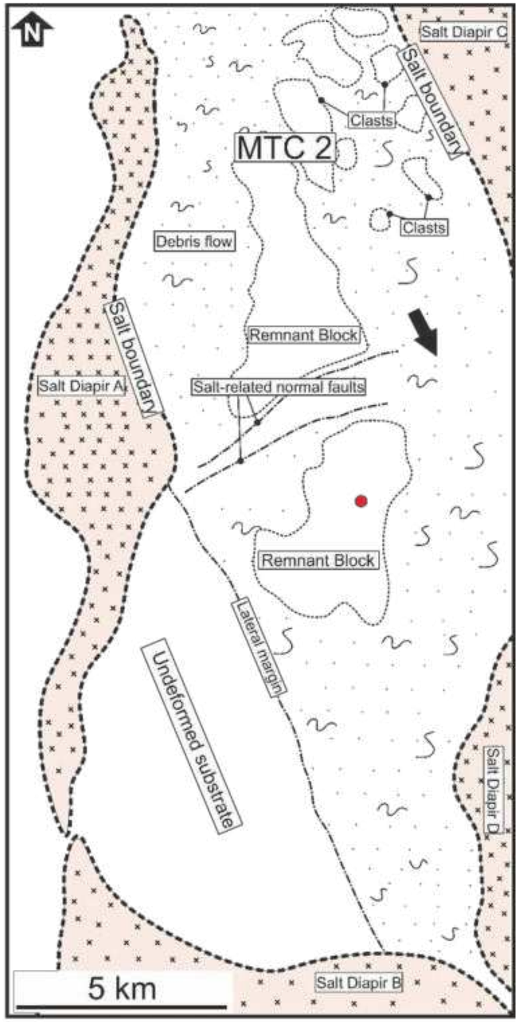

Figure 11c

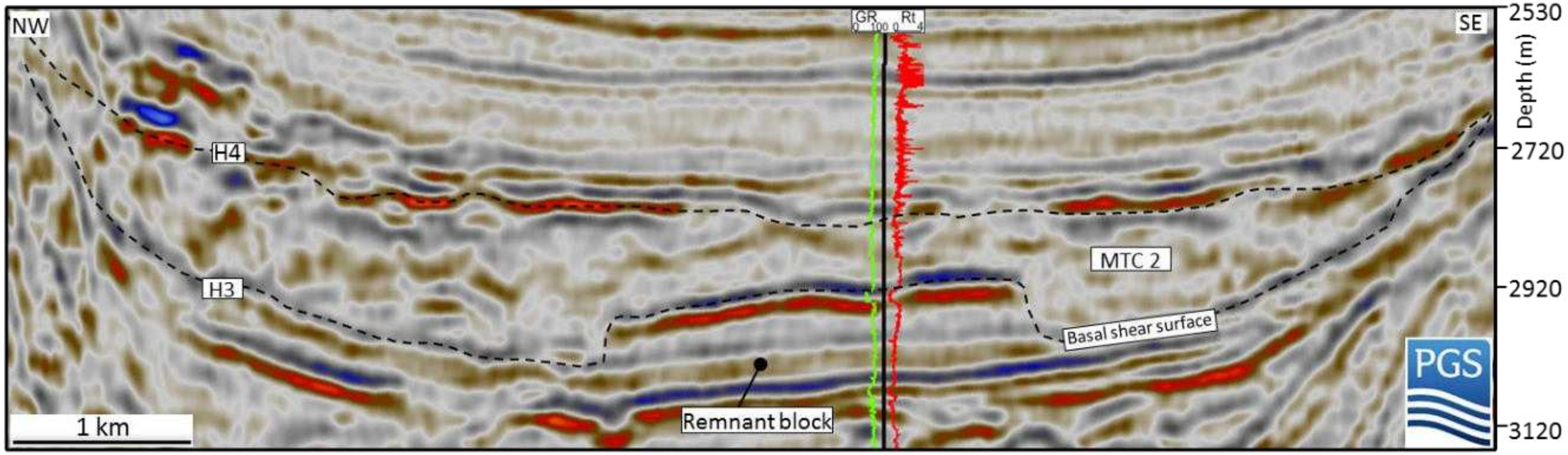
NW
SE
GR
0
100
0
Rt
4
H4
H3
MTC 2
Basal shear surface
Remnant block
1 km
PGS
2530
2720
2920
3120
Depth (m)

Figure 12a

Figure 12b

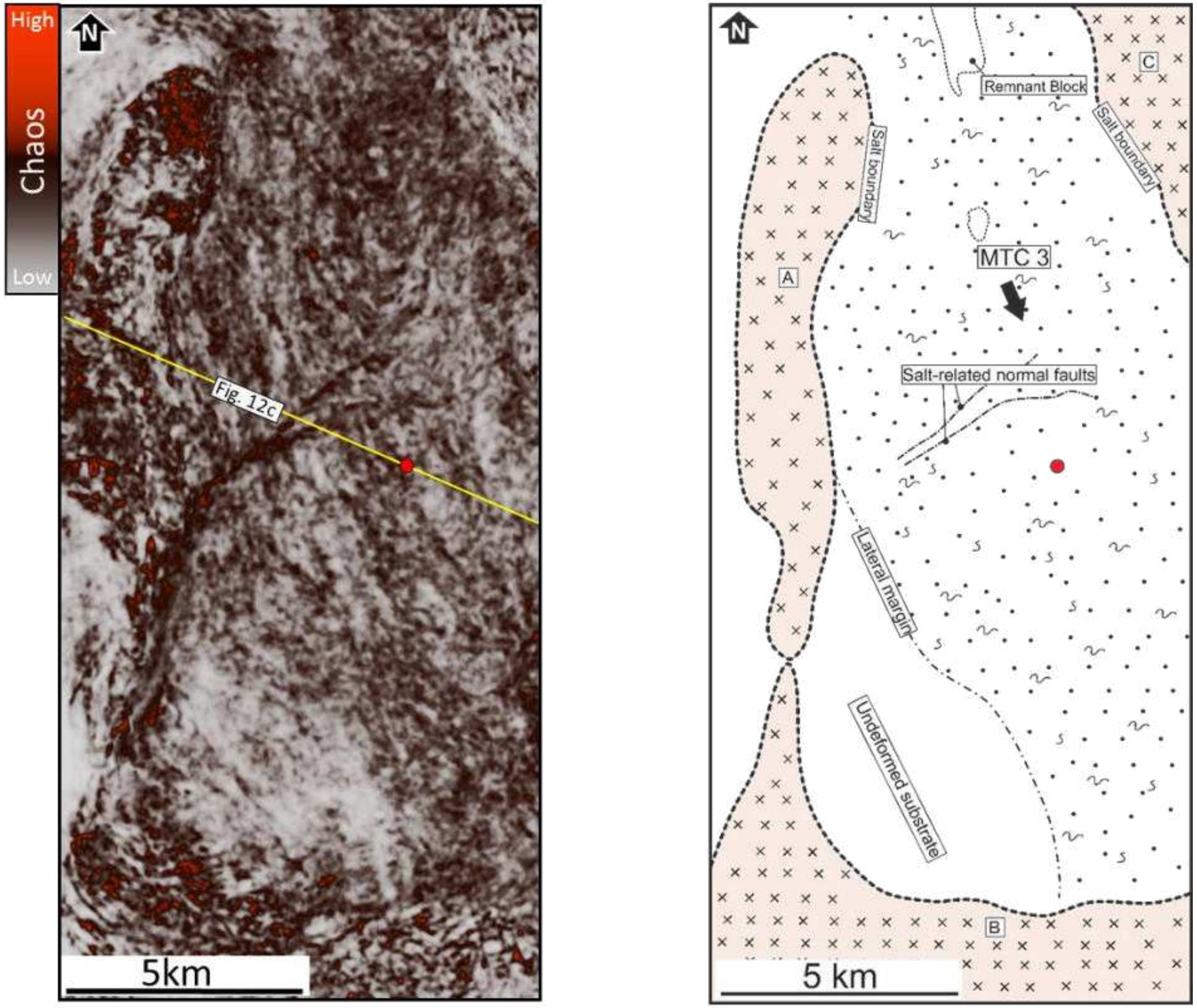
High
Chaos
Low
N
Fig. 12c
5km
N
Remnant Block
C
Salt boundary
Salt boundary
A
MTC 3
Salt-related normal faults
Lateral margin
Undeformed substrate
B
5 km

Figure 12c

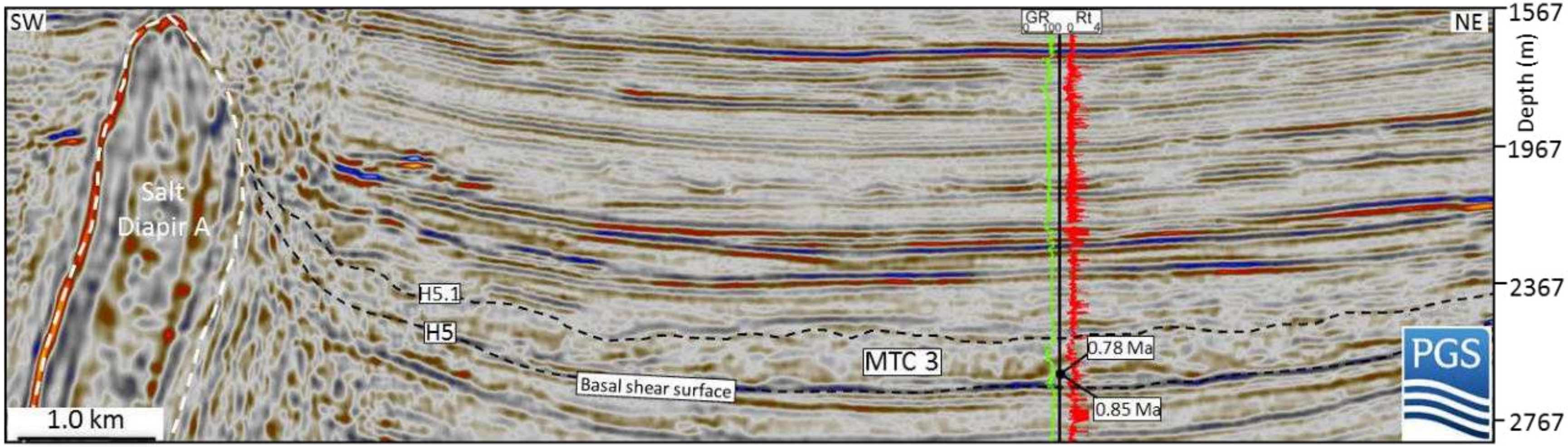
SW
NE
GR
0 100
Rt
0 4
1567
1967
2367
2767
Depth (m)
Salt
Diapir A
H5.1
H5
MTC 3
Basal shear surface
0.78 Ma
0.85 Ma
PGS
1.0 km

Figure 12d

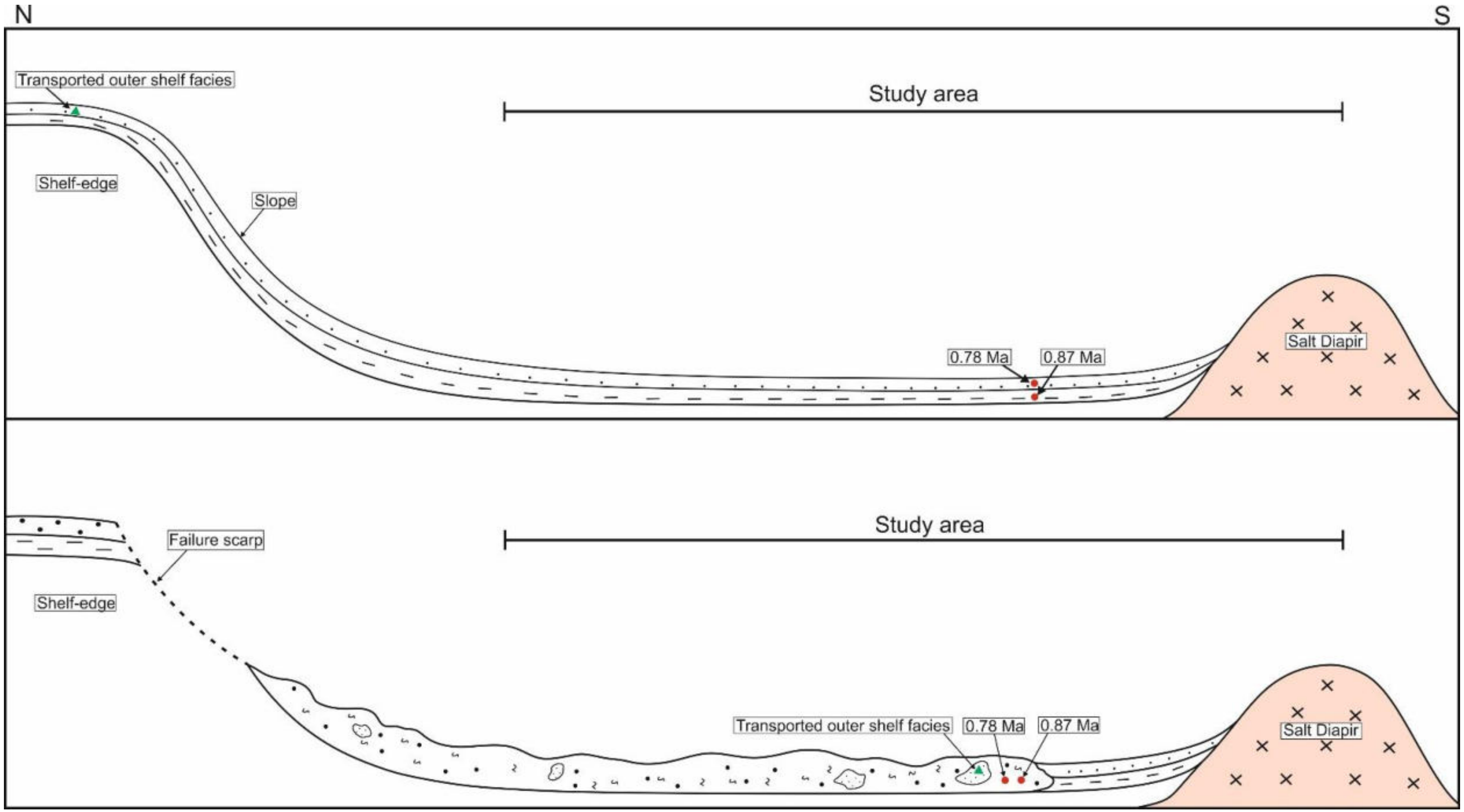

N
S
Transported outer shelf facies
Study area
Shelf-edge
Slope
Salt Diapir
0.78 Ma
0.87 Ma
Study area
Failure scarp
Shelf-edge
Transported outer shelf facies
0.78 Ma
0.87 Ma
Salt Diapir

Figure 12e

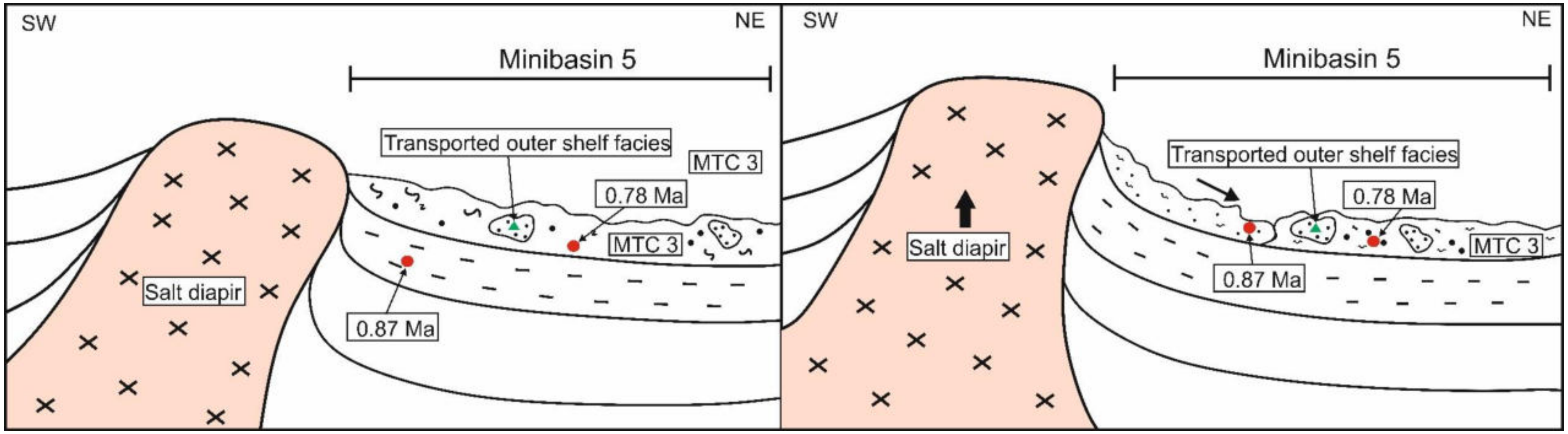
SW
NE
Minibasin 5
Transported outer shelf facies
MTC 3
0.78 Ma
MTC 3
Salt diapir
0.87 Ma
SW
NE
Minibasin 5
Transported outer shelf facies
0.78 Ma
Salt diapir
MTC 3
0.87 Ma

Figure 13

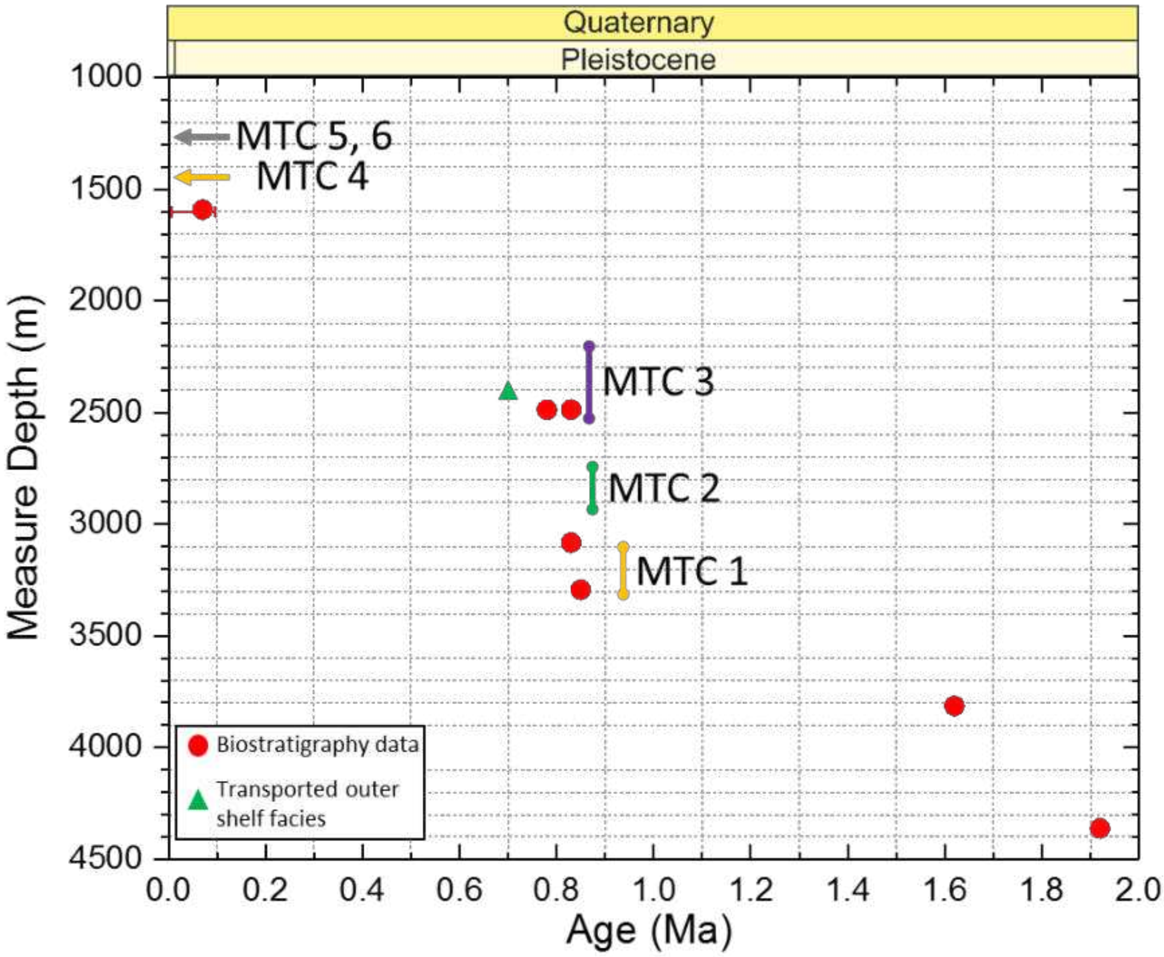
Quaternary
Pleistocene
MTC 5, 6
MTC 4
MTC 3
MTC 2
MTC 1
Biostratigraphy data
Transported outer shelf facies
Measure Depth (m)
Age (Ma)
1000
1500
2000
2500
3000
3500
4000
4500
0.0
0.2
0.4
0.6
0.8
1.0
1.2
1.4
1.6
1.8
2.0

Figure 14a

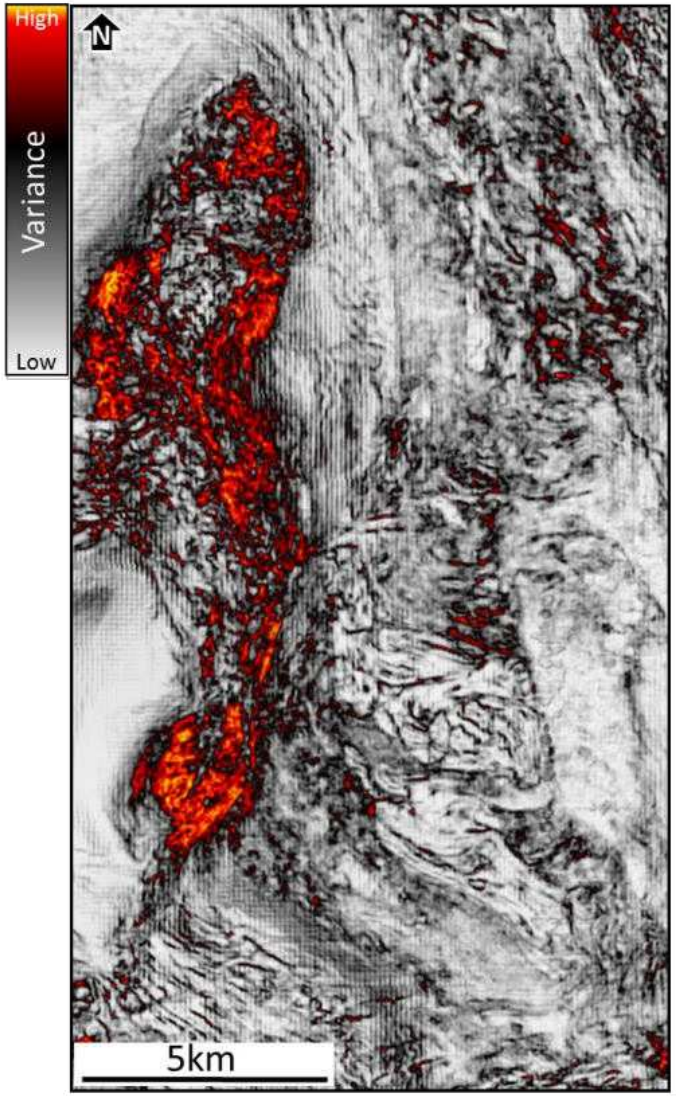

Figure 14b

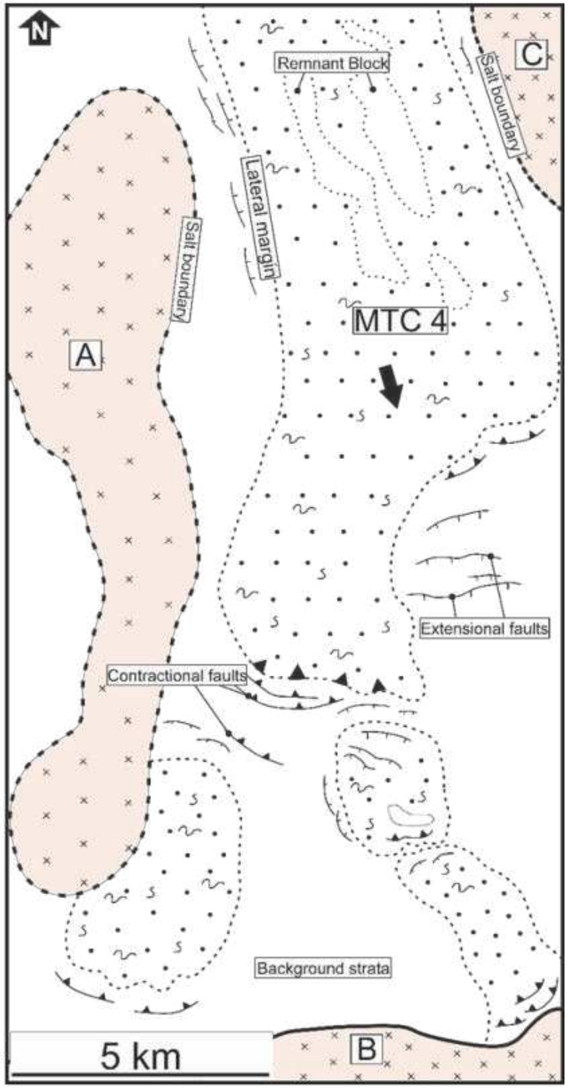

Figure 15a

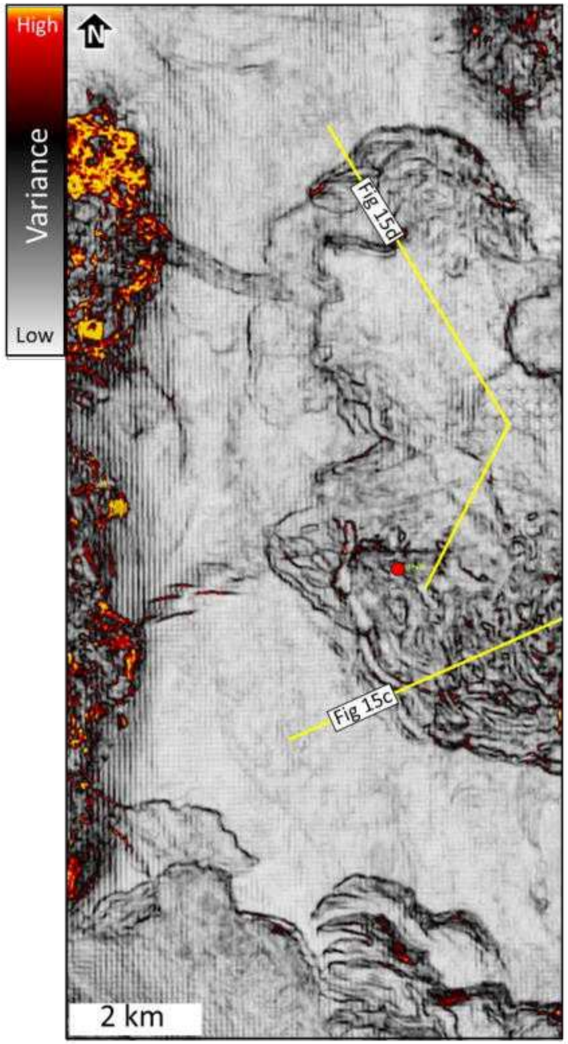

Figure 15b

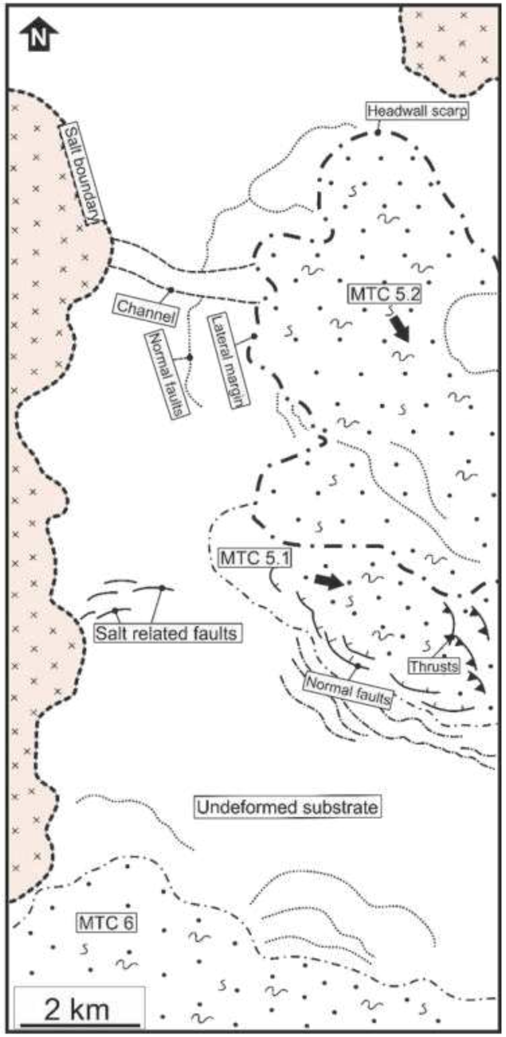

Figure15c

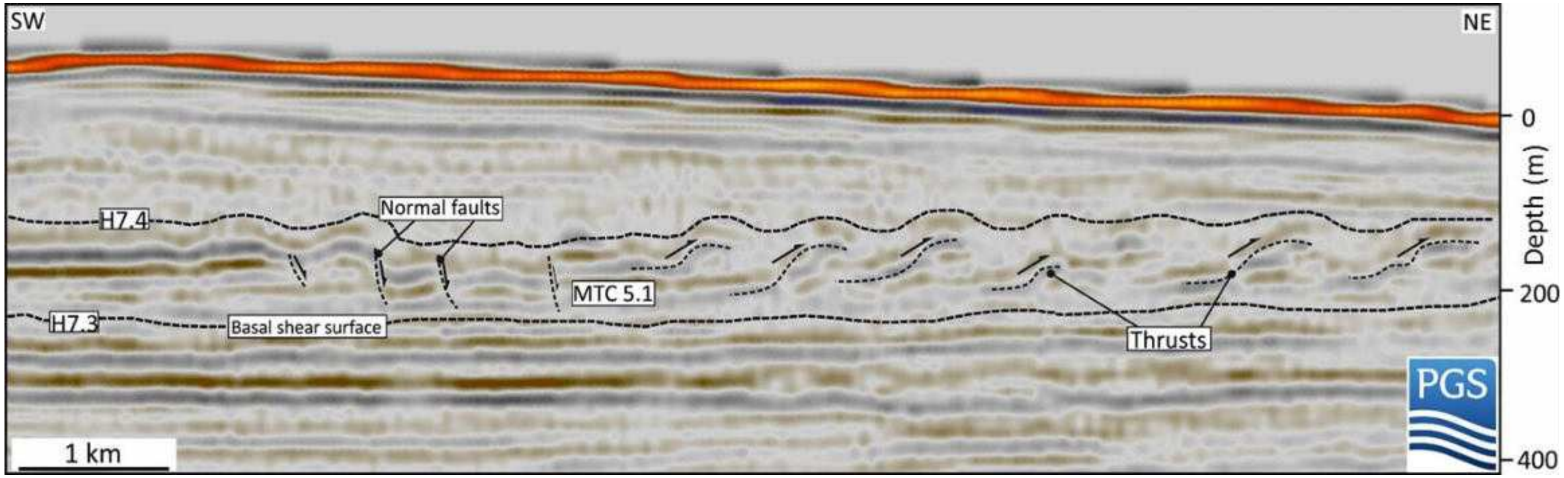

Figure 15d

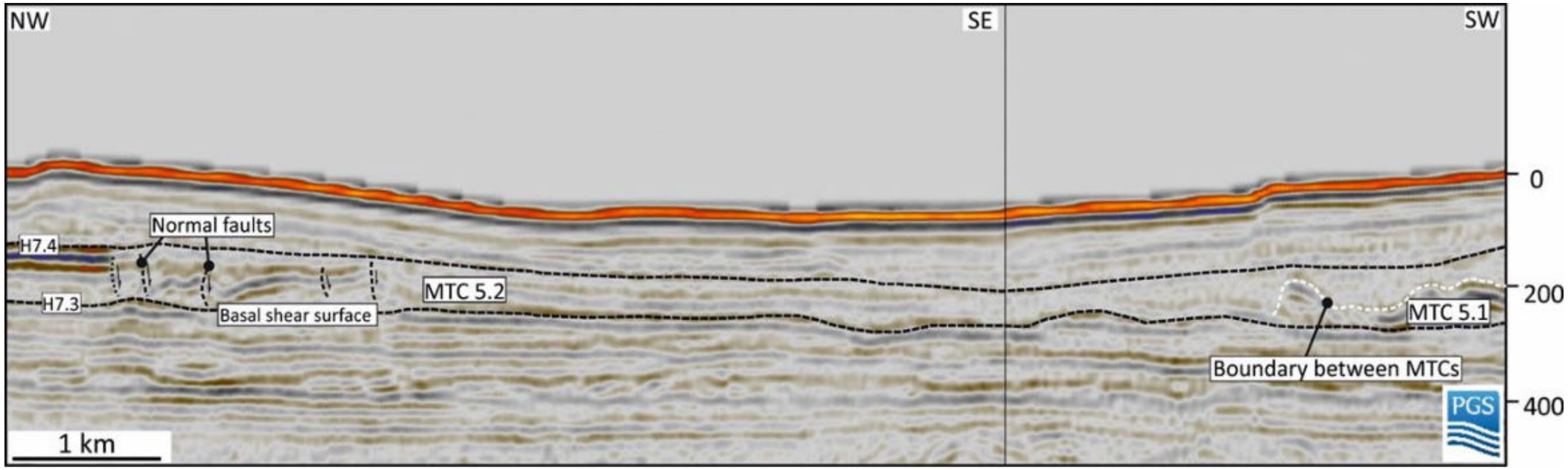

Figure 16a

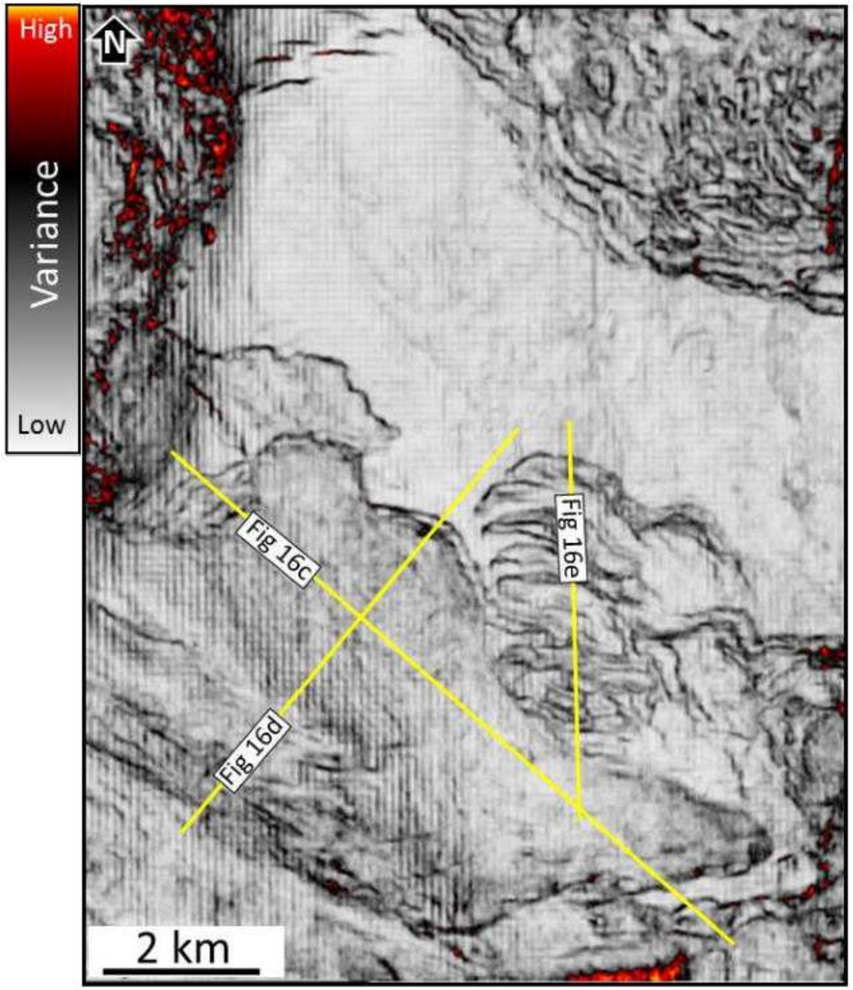

Figure 16b

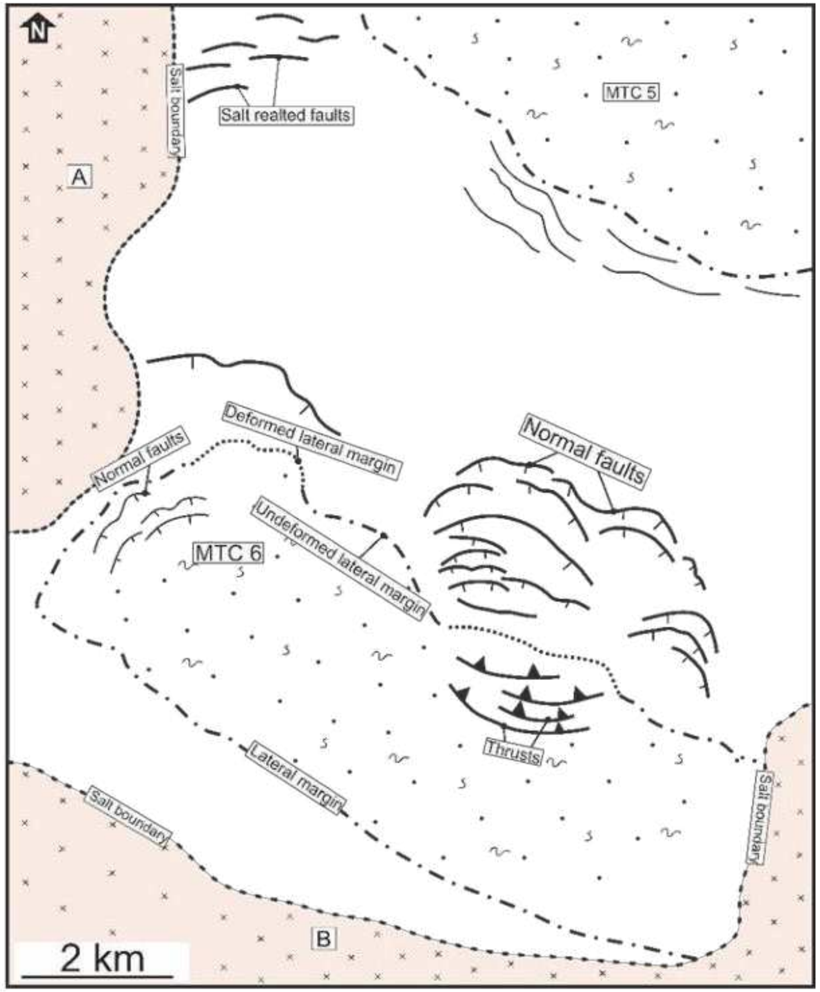

Figure 16c

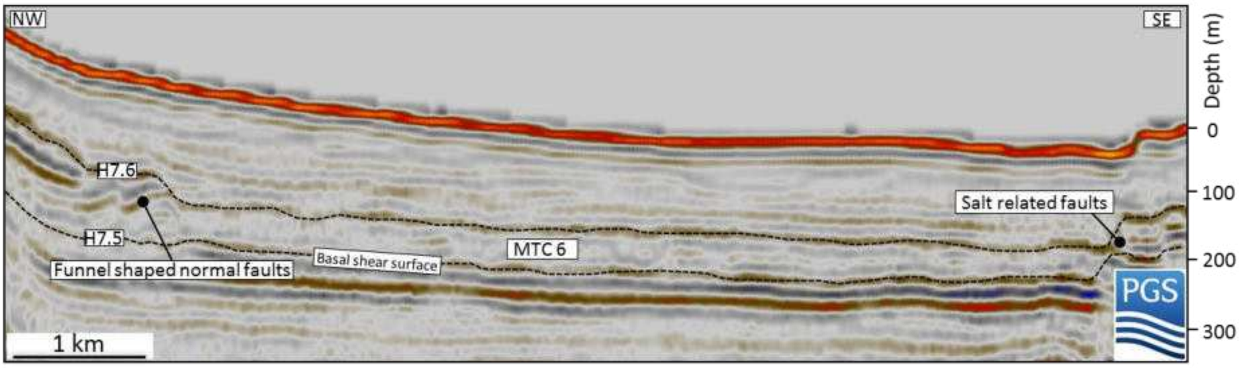

Figure 16d

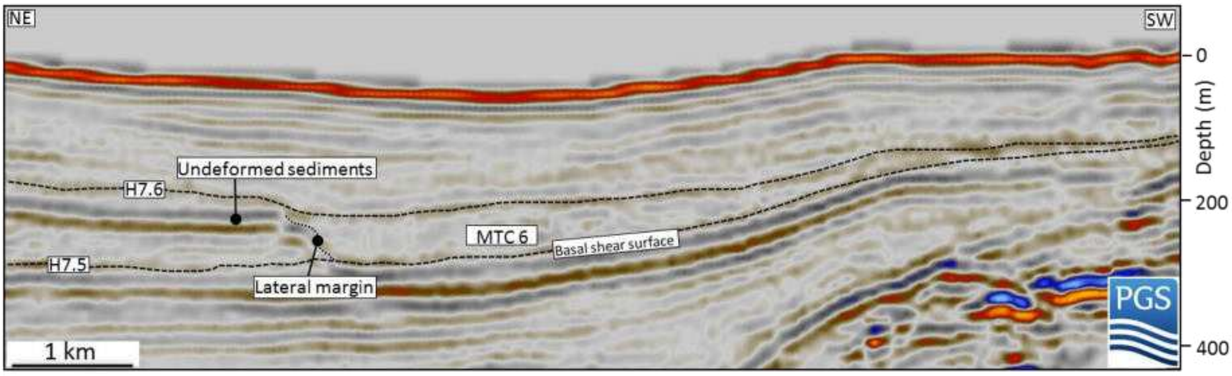

Figure 16e

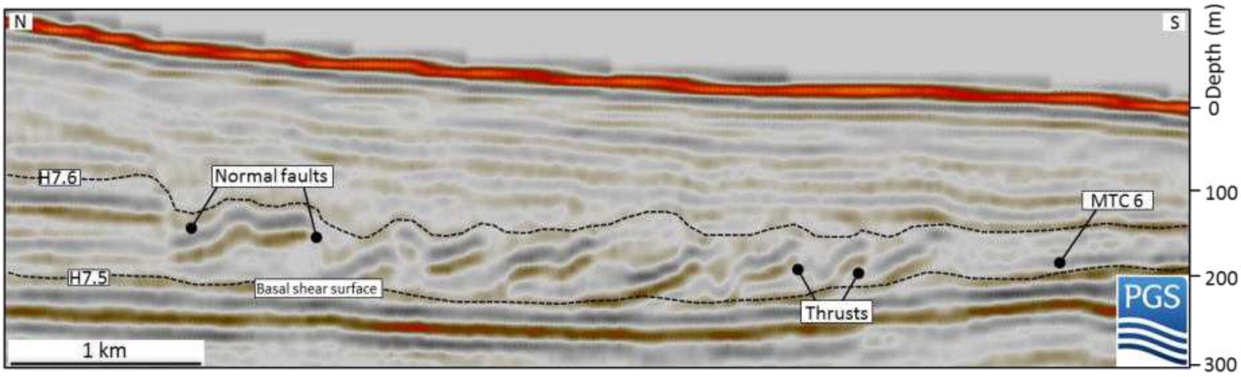

Figure 17a

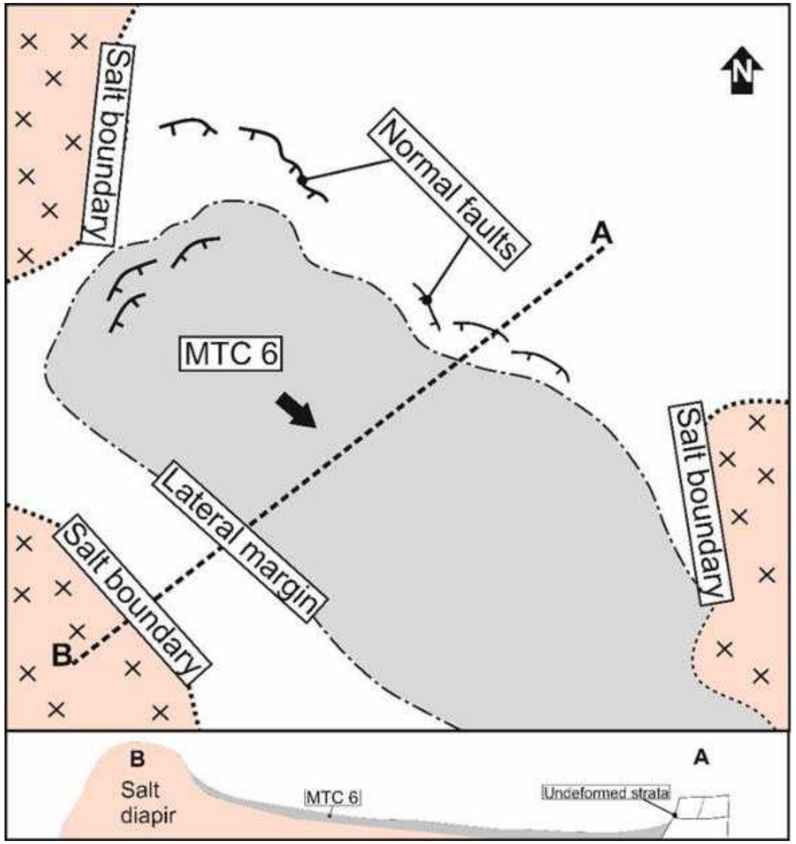

Figure 17b

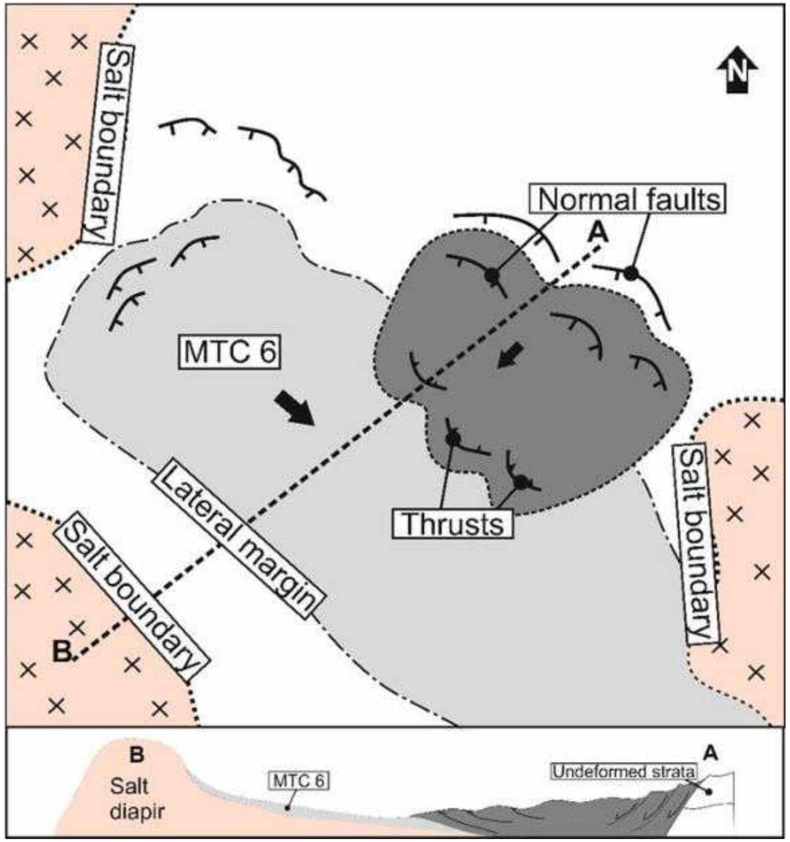

Figure 18

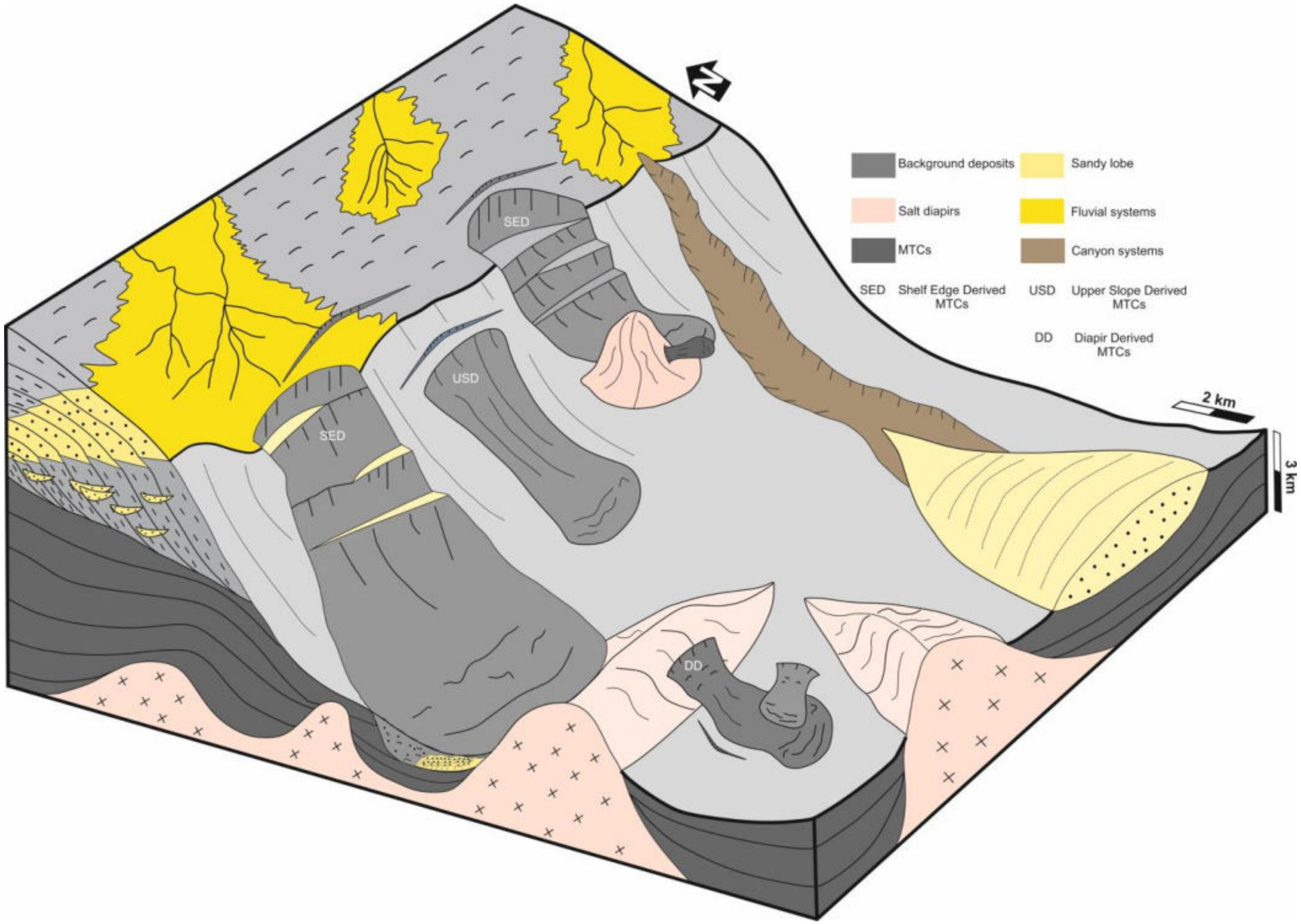
Background deposits
Sandy lobe
Salt diapirs
Fluvial systems
MTCs
Canyon systems
SED Shelf Edge Derived MTCs
USD Upper Slope Derived MTCs
DD Diapir Derived MTCs
2 km
3 km
SED
USD
SED
DD

Figure 19

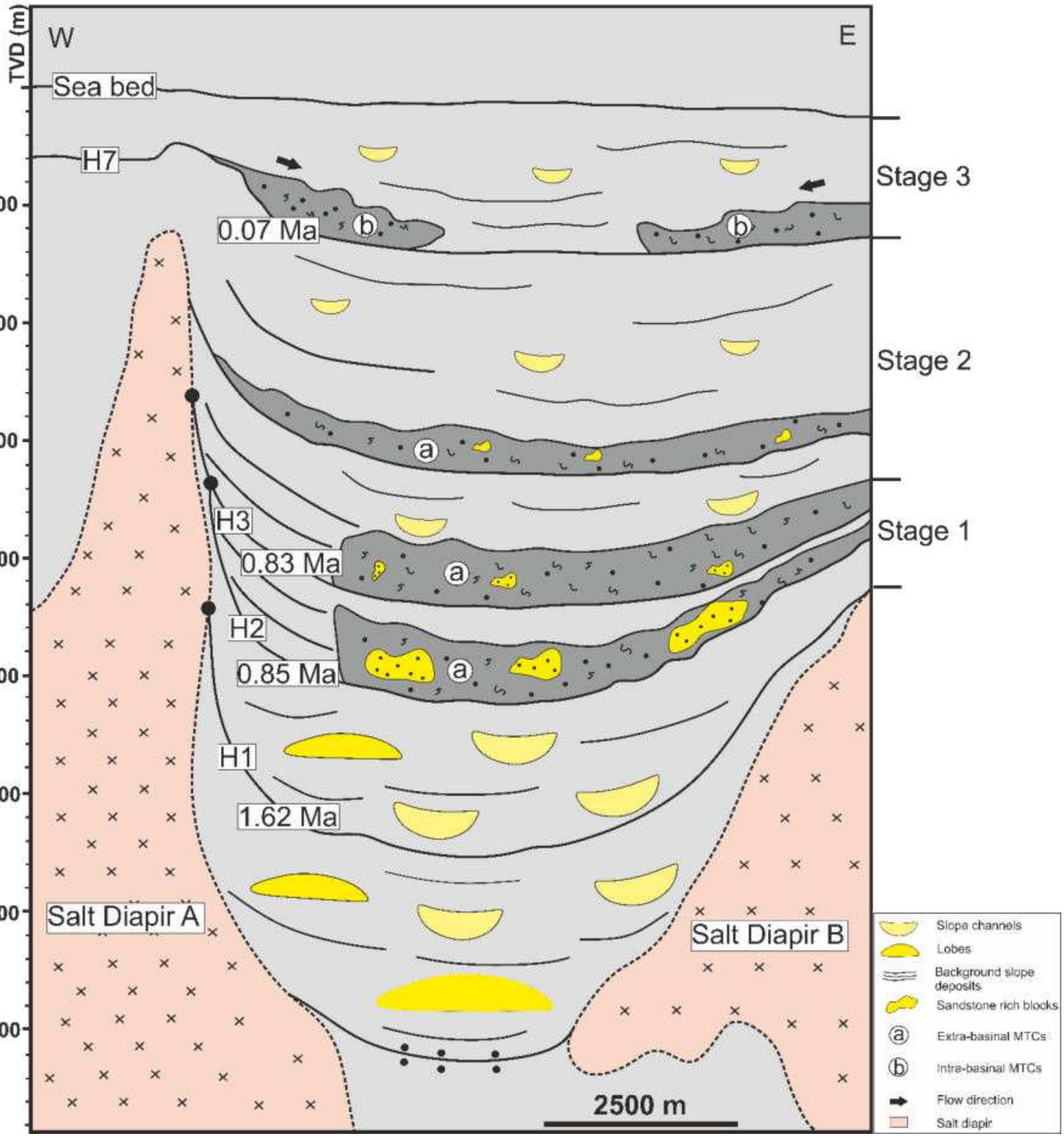
TVD (m)
W
E
Sea bed
H7
0.07 Ma
b
Stage 3
Stage 2
Stage 1
a
H3
0.83 Ma
H2
0.85 Ma
H1
1.62 Ma
500
1000
1500
2000
2500
3000
3500
4000
Salt Diapir A
Salt Diapir B
2500 m
Slope channels
Lobes
Background slope deposits
Sandstone rich blocks
Extra-basinal MTCs
Intra-basinal MTCs
Flow direction
Salt diapir

Figure 20

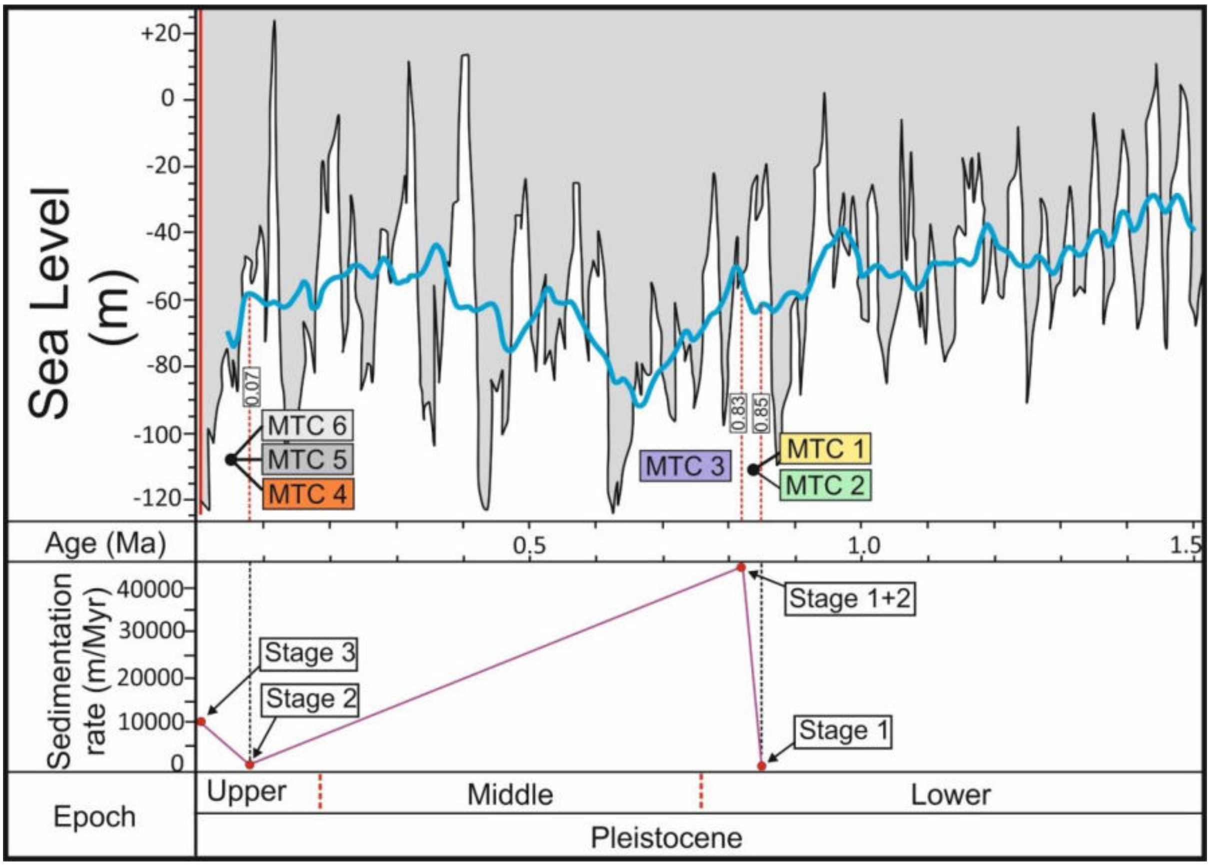

Sea Level (m)
+20
0
-20
-40
-60
-80
-100
-120
0.07
0.83
0.85
MTC 6
MTC 5
MTC 4
MTC 3
MTC 1
MTC 2
Age (Ma)
0.5
1.0
1.5
Sedimentation rate (m/Myr)
40000
30000
20000
10000
0
Stage 3
Stage 2
Stage 1+2
Stage 1
Epoch
Upper
Middle
Lower
Pleistocene